

# Remote Entanglement in Lattice Surgery: To Distill, or Not to Distill

Sitong Liu,<sup>1,2,3,\*</sup> John Stack,<sup>4,3</sup> Ke Sun,<sup>5,3</sup> Roel Van Beeumen,<sup>3</sup> Inder Monga,<sup>3</sup>  
Katherine Klymko,<sup>6</sup> Kenneth R. Brown,<sup>1,2,7,8</sup> and Erhan Saglamyurek<sup>3,5,†</sup>

<sup>1</sup>*Duke Quantum Center, Duke University, Durham, NC 27701, USA*

<sup>2</sup>*Department of Electrical and Computer Engineering, Duke University, Durham, NC 27708, USA*

<sup>3</sup>*Lawrence Berkeley National Laboratory, Berkeley, CA 94720, USA*

<sup>4</sup>*Department of Computer Science, North Carolina State University, Raleigh, NC 27606, USA*

<sup>5</sup>*University of California, Berkeley, CA 94720, USA*

<sup>6</sup>*National Energy Research Scientific Computing Center,*

*Lawrence Berkeley National Laboratory, Berkeley, CA 94720, USA*

<sup>7</sup>*Department of Physics, Duke University, Durham, NC 27708, USA*

<sup>8</sup>*Department of Chemistry, Duke University, Durham, NC 27708, USA*

(Dated: March 9, 2026)

Distributed quantum computing can potentially address the scalability challenge by networking processors through photon-mediated remote entanglement. Prior approaches assumed that remote Bell pairs require distillation, resulting in substantial overhead, to achieve sufficiently high fidelity before use. However, recent results show that lattice-surgery operations at logical qubit boundaries tolerate significantly higher error rates than previously assumed. We quantify the resource trade-offs between distillation overhead and surface-code distance requirements under realistic constraints including probabilistic entanglement generation and memory decoherence. We identify the fidelity crossover point separating the two regimes and show that choosing the right strategy can reduce resource overhead by up to two orders of magnitude at low fidelities and up to 68% at high fidelities. We briefly describe the application of these methods to ion-trap and neutral-atom platforms. These results provide co-design principles for optimizing photonic interconnects and fault-tolerant architectures in distributed quantum computers.

## I. INTRODUCTION

As quantum processors scale, building ever-larger single-chip devices becomes increasingly difficult due to practical hardware limits such as chip area, control crosstalk, and thermal and optical routing constraints. Modular or distributed quantum computing (DQC) addresses these challenges by networking multiple medium-scale processors through photonic entanglement links. In such architectures, fault tolerance is typically provided by quantum error correction (QEC), while nonlocal logical operations are mediated by shared Bell pairs used for teleportation [1–5].

The achievable performance in DQC is jointly constrained by local noise within each module and by the fidelity, availability, and consumption of entanglement distributed between modules. Moreover, conventional approaches to fault-tolerant distributed operation typically assume that raw Bell pairs must undergo entanglement distillation [6] before use, as the Bell-pair fidelity is often lower than the fault-tolerance threshold of the code [7–9], thereby incurring substantial overhead. Dedicated distillation factories and ancillary communication qubits can consume a substantial fraction of a module’s physical resources, motivating the search for regimes in which distillation can be bypassed.

A recent insight fundamentally changes this picture.

QEC simulations show that errors at surface-code patch interfaces have significantly higher fault-tolerance thresholds during lattice surgery. These thresholds are approximately one order of magnitude higher than errors within individual code patches. For example, using a circuit-level noise model, studies show a Bell-pair error threshold of 15.3% for remote gate teleportation when local physical noise is 0.1% [10]. This asymmetric tolerance means moderate-fidelity Bell pairs may suffice for remote lattice surgery without prior purification, forming the basis for the distillation-free approach we examine here.

However, whether this regime is practically accessible depends on concrete operational constraints. Prior studies of modular and distributed architectures often model inter-node links as effective logical channels with fixed rate and error parameters. This simple assumption hides a fundamental conflict that entanglement between modules is generated probabilistically and must be consumed within well-defined operational windows set by QEC cycles. Under these constraints, the feasibility of distributed surface-code operations depends sensitively on how many raw Bell pairs are required per remote lattice surgery measurement, how their fidelity evolves during buffering and use, and how many logical patches and communication resources can be hosted within each processor, etc. These constraints become particularly strict in regimes that seek to avoid entanglement distillation, where raw Bell pairs are consumed directly without intermediate purification.

In this work, we establish the intrinsic crossover boundary that determines where distillation-free and

\* sitong.liu@duke.edu

† esaglamyurek@lbl.gov

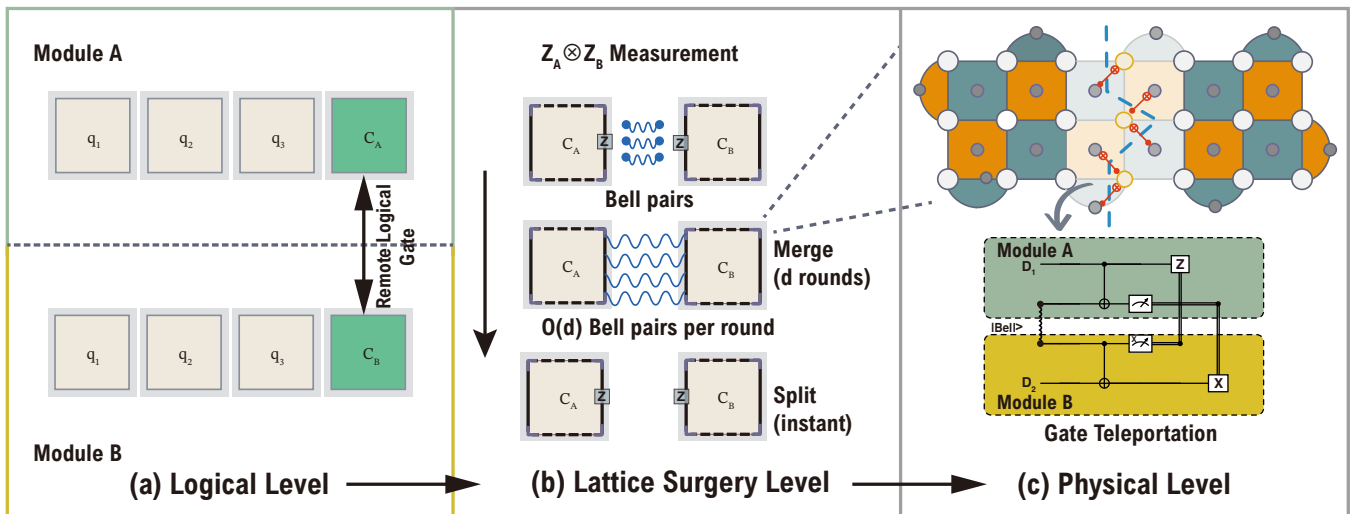


FIG. 1. **Remote lattice surgery for distributed architecture.** (a) Logical level: Modules A and B are physically separated and perform remote operations on encoded logical qubits through communication qubits (green) via Pauli product measurements. (b) Lattice surgery level:  $Z \otimes Z$  measurements between logical qubits  $C_A$  and  $C_B$  are implemented via merge-split of the logical qubit boundaries. The merge operation requires  $d$  syndrome measurement rounds, where  $d$  is the surface code distance, consuming  $\mathcal{O}(d)$  Bell pairs per round. The split operation is instantaneous as it coincides with the standard syndrome measurement cycle. (c) Physical level: Top illustrates the merge operation between two surface code patches encoding logical qubits  $q_1$  (left) and  $q_2$  (right). Data qubits are shown as white circles and stabilizer plaquettes as colored regions. The light yellow circles and faded areas represent ancilla qubits and additional stabilizers generated during merging. Blue dashed lines indicate the physical module boundaries. Bottom shows the gate teleportation circuit with Bell pair. The Bell pairs connect the interface regions to enable the remote CNOT operations (highlighted in red in the top panel).

distillation-assisted architectures are respectively favorable. Strict physical trade-offs among Bell-pair consumption, Bell-pair fidelity, and local processor size dictate this boundary. By mapping out these boundaries, we provide quantitative guidance for designing modular surface-code architectures that balance hardware complexity against achievable logical performance. Within the distillation-free parameter regimes identified here, directly consuming raw Bell pairs reduces communication-qubit overhead while preserving the logical connectivity required for lattice surgery. These results clarify when each approach is viable in distributed surface-code architectures and highlight the key trade-offs that must be considered in the co-design of photonic interconnects and fault-tolerant logical layouts.

## II. FAULT-TOLERANT REQUIREMENTS FOR REMOTE LATTICE SURGERY

We consider  $K$  modules  $\mathcal{M} = \{M_1, \dots, M_K\}$  interconnected by network  $\mathcal{G} = (\mathcal{M}, E)$ , where each module  $M_i$  hosts logical qubits encoded in distance- $d$  rotated surface codes. We derive the entanglement resource requirements, consumption rates, and fidelity thresholds that govern whether direct consumption of raw Bell pairs suffices for fault tolerance.

### A. Remote lattice surgery protocol

Logical gates in the rotated surface-code lattice-surgery framework are realized through Pauli product measurements (PPMs): adjacent patches (distance  $d$ ,  $d^2$  physical qubits each) can be merged directly along their shared boundary, or connected through an ancilla patch for multi-qubit and long-range operations. In either case, a merge-measure-split sequence with  $d$  syndrome rounds of stabilizer measurement is required to extract the joint parity at full code distance. The measurement projects the participating qubits onto the  $+1$  or  $-1$  eigenspace of the target multi-qubit Pauli product operator, with measurement outcomes determining Pauli corrections that are tracked classically. In the Pauli-based computation framework, all Clifford+ $T$  circuits reduce to a sequence of such PPMs, where each non-Clifford  $T$  gate consumes one magic state and one PPM [11]. We refer the reader to Refs. [11–14] for a detailed description.

For intra-module operations, seam stabilizers are measured with local gates. For inter-module operations, seam stabilizers span physically separated hardware, and remote parity checks require Bell pairs shared between modules [1, 10].

## B. Bell-pair generation: mechanism and rates

Remote entanglement is established via *heralded photonic links* [15–18]: a coincident detection event at a Bell-state analyzer heralds successful projection into an entangled Bell state [19], with overall success probability  $p_{\text{herald}} \ll 1$ .

The post-heralded fidelity  $F_{\text{Bell}}$  is governed by distinct physical mechanisms: Hong-Ou-Mandel visibility, channel losses, detector dark counts [20], and qubit decoherence during the heralding window [17]. Distributed Bell pairs are typically an order of magnitude noisier than local operations [21–23]. We treat  $F_0 = 1 - p_{\text{raw}}$  as a configurable input informed by experimental benchmarks rather than deriving it from physical-layer parameters.

Scalability is jointly limited by two hardware characteristics: (i) the *generation rate*  $\lambda$  (pairs available per QEC cycle) and (ii) the *fidelity*  $F_0$ , which must exceed the fault-tolerance threshold. Each module  $M_k$  carries  $I_k$  optical interfaces [18, 24, 25] which together determine its total Bell-pair generation rate  $\lambda_k$ .

## C. Bell-pair consumption per seam measurement

The Bell-pair cost of a distributed logical operation depends on both the circuit realization of the non-local stabilizer measurement and the code distance  $d_s$  required to suppress logical errors to the target level.

*a. Bell pairs per syndrome round.* Each round of remote stabilizer measurement couples  $\mathcal{O}(d_s)$  boundary qubits via distributed entanglement [1, 11], consuming

$$n^{\text{round}} = ad_s - c \quad (1)$$

Bell pairs, where  $a$  and  $c$  are protocol-dependent constants. Gate-teleportation implementations, which replace interface-crossing two-qubit gates with teleported gates, give  $(a, c) = (2, 1)$  (see Fig. 1(c)), yielding approximately  $2d_s - 1$  Bell pairs per round [10]. Alternatively, measurement-teleportation and Bell-measurement schemes reduce this overhead to approximately  $d_s$  to  $2d_s$  pairs per round [1, 4].

*b. Bell pairs per logical operation.* Because fault tolerance requires each joint lattice-surgery measurement to be repeated for  $d_s$  consecutive syndrome-extraction rounds, each logical two-qubit operation spans  $d_s$  logical cycles [11]. The total Bell-pair consumption per logical operation is therefore

$$N_{\text{QEC}} = d_s \cdot n^{\text{round}} = ad_s^2 - cd_s = \mathcal{O}(d_s^2). \quad (2)$$

## D. Seam error threshold

Recent studies have characterized the fault-tolerance properties of seam operations in distributed surface

codes. Numerical simulations reveal that syndrome extraction at the interface tolerates error rates approximately one order of magnitude higher than bulk operations [2]. This is because errors from noisy Bell pairs propagate only along a single spatial dimension of the surface code during lattice surgery, limiting the number of paths through which errors can form logical failures [2].

For the unrotated surface code under a phenomenological noise model, the thresholds are approximately  $p_{\text{bulk}}^* \approx 1\%$  and  $p_{\text{seam}}^* \approx 10\%$  [2]. For the rotated surface code (Figure 1 (b)), circuit-level simulations confirm similar threshold behavior [1, 3, 4]. Under an amplification factor  $\Gamma = p_{\text{seam}}/p_{\text{bulk}} = 10$ , fault tolerance persists with  $p_{\text{bulk}}^* \approx 0.73\%$  and  $p_{\text{seam}}^* \approx 7.3\%$  [3]. Other teleportation protocols report Bell-pair error thresholds ranging from  $p_{\text{Bell}}^* \approx 17\%$  to  $30\%$ , while local gate errors must remain below approximately  $0.1\%$  to  $0.7\%$  [1, 4].

## III. DISTILLATION TRADE-OFF UNDER STATIC FIDELITY

To distill or not to distill, that is the question.

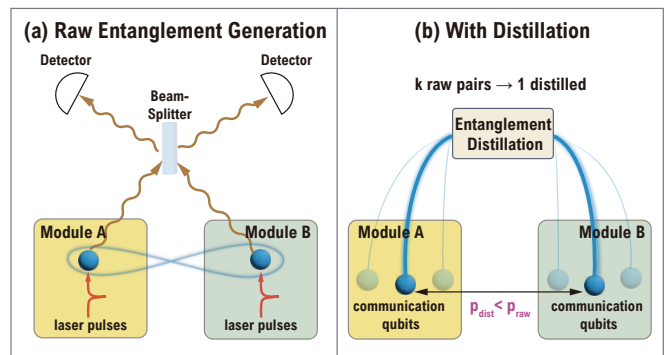


FIG. 2. **Comparison of remote entanglement utilization schemes.** (a) Direct use of raw Bell pairs. Heralded entanglement is generated via optical links between communication qubits in Module A and B, with link error  $p_{\text{raw}}$ . (b) Distillation-based approach.  $n_{\text{pairs}}$  raw Bell pairs are consumed by an entanglement distillation protocol  $D$  to produce a single high-fidelity Bell pair with error  $p_{\text{eff}} < p_{\text{raw}}$ .

We now quantify when direct consumption of raw Bell pairs is resource-optimal over distillation, as a function of Bell-pair fidelity, code distance, and purification overhead.

### A. Fitted model for code distance requirements

To quantify the relationship between Bell-pair fidelity and surface-code distance, we adopt the logical error model and fitted values from Sunami *et al.* [10]. For a distance- $d_s$  rotated surface code undergoing remote lattice surgery with Bell-pair error rate  $p_{\text{Bell}}$  and local gate

error rate  $p_{\text{local}}$ , the logical error rate per syndrome extraction round is given by

$$p_L = \kappa(d_s + 1)^\eta \left[ A^{\frac{d_s+1}{2}} + B^{\frac{d_s+1}{2}} + \sum_{\gamma_s=1}^{d_s} (AM^2)^{\gamma_s/2} B^{\frac{d_s+1-\gamma_s}{2}} \right], \quad (3)$$

where  $A = p_{\text{Bell}}/p_{\text{th}}^{\text{Bell}}$ ,  $B = p_{\text{local}}/p_{\text{th}}^{\text{local}}$ , and  $M = 1 + \alpha_c p_{\text{local}} p_{\text{th}}^{\text{Bell}} / (1 - \sqrt{B})$ . The model parameters, obtained from circuit-level simulations, are  $\kappa = 5.44 \times 10^{-2}$ ,  $\eta = 5.34 \times 10^{-1}$ ,  $\alpha_c = 3.15 \times 10^2$ ,  $p_{\text{th}}^{\text{Bell}} = 15.3\%$ , and  $p_{\text{th}}^{\text{local}} = 1.02\%$ . Note that in practice, the cross terms in Eq. (3) reduce the effective Bell-pair error threshold to  $p_{\text{th}}^{\text{Bell}} = p_{\text{th}}^{\text{Bell}}/M^2 \approx 13.36\%$  ( $F_0 \approx 86.64\%$ ), below the nominal fitted value of 15.3%.

For a target logical error rate  $p_L^{\text{target}}$  and a given local error rate  $p_{\text{local}}$  (fixed to 0.1% throughout), we define the minimum required surface-code distance as

$$d_s^*(p_{\text{Bell}}) = \min_{\substack{d_s \in 2\mathbb{N}+1 \\ d_s \geq 3}} \left\{ d_s : p_L(d_s, p_{\text{Bell}}, p_{\text{local}}) \leq p_L^{\text{target}} \right\}, \quad (4)$$

where  $p_L(\cdot)$  denotes the logical error-rate model. In practice,  $d_s^*$  is obtained via binary search over odd code distances.

This formulation captures a critical trade-off: as  $p_{\text{Bell}}$  approaches the threshold  $p_{\text{th}}^{\text{Bell}}$  (i.e.,  $A \rightarrow 1$ ), maintaining the target  $p_L^{\text{target}}$  requires rapidly increasing  $d_s^*$ . With  $p_{\text{local}} = 0.1\%$  and  $p_L^{\text{target}}$  fixed, this scaling is determined by the pure Bell-pair term  $A^{(d_s+1)/2}$  in Eq. (3), where  $A = p_{\text{Bell}}/p_{\text{th}}^{\text{Bell}}$ . The largest cross term ( $\gamma_s = d_s$ ),  $(AM^2)^{d_s/2} B^{1/2}$ , does not alter the leading scaling with  $p_{\text{Bell}}$ , since  $M$  and  $B$  are independent of  $d_s$  and therefore only modify the overall prefactor of the exponential dependence set by  $A^{(d_s+1)/2}$ .

Inverting the leading exponential dependence gives

$$d_s^* \propto \frac{1}{\log(p_{\text{th}}^{\text{Bell}}/p_{\text{Bell}})}, \quad (5)$$

which diverges as  $p_{\text{Bell}} \rightarrow p_{\text{th}}^{\text{Bell}}$  and saturates at its minimum when  $p_{\text{Bell}} \ll p_{\text{th}}^{\text{Bell}}$ . Since the per-round Bell-pair consumption scales as  $n^{\text{round}} \propto d_s$ , the total resource overhead grows correspondingly as the threshold is approached.

Although the numerical coefficients in Eq. (3) are specific to the fitted model of Ref. [10], the exponential suppression and threshold asymmetry are generic features confirmed by independent simulations [1, 2]. In the standard surface-code threshold argument [26], the logical error rate per round scales as  $p_L \sim (p/p_{\text{th}})^{\lfloor (d+1)/2 \rfloor}$ . In a distributed architecture, Bell-pair noise enters only through teleported stabilizer measurements along the inter-module seam and propagates to a single column of qubits rather than the full two-dimensional bulk [2], which is why  $p_{\text{th}}^{\text{Bell}} \gg p_{\text{th}}^{\text{local}}$  in Eq. (3).

## B. Distillation Protocols and Distance Scaling

Entanglement distillation improves Bell-pair fidelity by consuming multiple noisy pairs to produce a single purified pair, enabling either the use of otherwise unsuitable raw links or the reduction of code distance requirements for a given raw fidelity. A distillation protocol  $\mathcal{D}$  consumes  $n_{\text{pairs}}$  raw Bell pairs with error rate  $p_{\text{raw}}$  and probabilistically outputs one purified pair with improved fidelity, characterized by two mappings:

$$p_{\text{out}} = f_{\mathcal{D}}(p_{\text{raw}}), \quad p_{\text{succ}} = g_{\mathcal{D}}(F_0; p_{\text{local}}), \quad (6)$$

where  $p_{\text{out}}$  is the output error rate,  $p_{\text{succ}}$  is the success probability,  $F_0 = 1 - p_{\text{raw}}$  is the raw fidelity (post-heralded Bell-pair fidelity), and  $p_{\text{local}}$  captures local gate and measurement errors during the distillation circuit. The input consumption  $n_{\text{pairs}}$  is protocol-dependent.

The effective Bell-pair error rate entering seam syndrome extraction is

$$p_{\text{Bell}}^{\text{eff}} = \begin{cases} p_{\text{raw}}, & \text{(no distillation),} \\ f_{\mathcal{D}}(p_{\text{raw}}), & \text{(with protocol } \mathcal{D}), \end{cases} \quad (7)$$

denoted  $p_{\text{eff}}$  for brevity. Since the logical error model Eq. (3) is monotonically non-decreasing in  $p_{\text{Bell}}$ , the required code distance  $d_s^*(p_{\text{Bell}})$  inherits this monotonicity. Any effective distillation protocol therefore satisfies  $p_{\text{eff}} < p_{\text{raw}}$  and enables a distance reduction

$$\Delta d_s = d_s^*(p_{\text{raw}}) - d_s^*(p_{\text{eff}}) \geq 0, \quad (8)$$

decreasing the per-round Bell-pair consumption from  $ad_s^*(p_{\text{raw}}) - c$  to  $ad_s^*(p_{\text{eff}}) - c$ . We quantify this reduction through the distance ratio

$$\rho(p_{\text{raw}}) = \frac{d_s^*(p_{\text{eff}})}{d_s^*(p_{\text{raw}})}, \quad (9)$$

where  $\rho \in (0, 1)$ , with smaller values indicating greater distance savings. This per-round reduction must however be weighed against the multiplicative overhead  $n_{\text{pairs}}/p_{\text{succ}}$  required to produce each purified pair. The quantitative distance reductions achieved by representative protocols are shown in Fig. 3. Since  $d_s^*$  already exceeds 400 at  $F_0 = 87\%$ , we restrict our analysis to  $F_0 \geq 90\%$ , which covers all near-term experimentally relevant fidelities.

## C. Expected Bell-pair consumption under probabilistic distillation

Entanglement distillation reduces the required code distance from  $d_s^*(p_{\text{raw}})$  to  $d_s^*(p_{\text{eff}})$ , lowering the per-round purified pair requirement to  $n^{\text{round}}(p_{\text{eff}}) = ad_s^*(p_{\text{eff}}) - c$ . However, producing each purified pair requires  $n_{\text{pairs}}$  raw pairs per attempt and succeeds only with probability  $p_{\text{succ}} = g_{\mathcal{D}}(F_0; p_{\text{local}})$ , so the total raw consumption carries a multiplicative overhead.

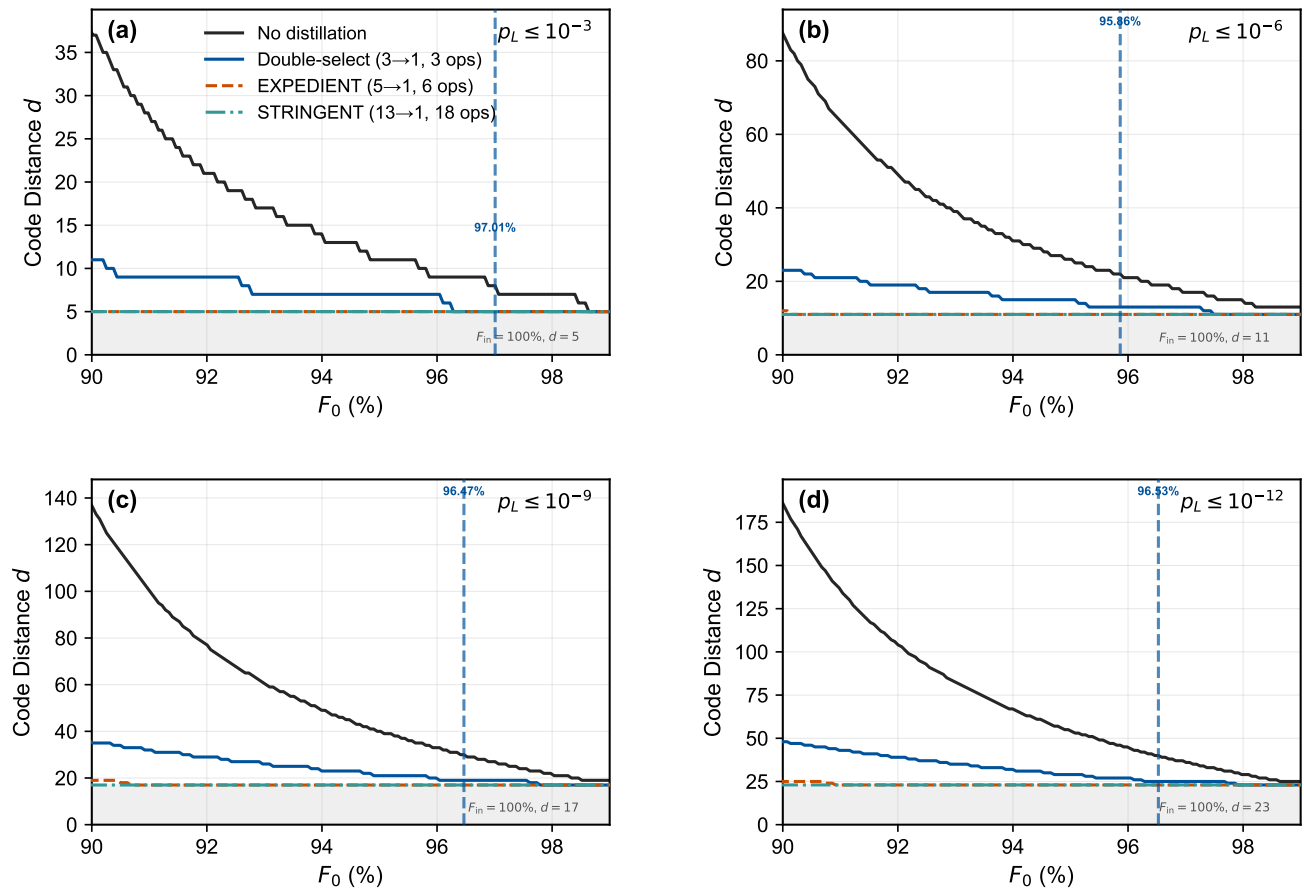


FIG. 3. Required surface-code distance  $d$  for remote lattice surgery versus raw Bell-pair fidelity  $F_0$ , at target logical error rates (a)  $p_L \leq 10^{-3}$ , (b)  $10^{-6}$ , (c)  $10^{-9}$ , (d)  $10^{-12}$ . The no-distillation baseline (black solid) is compared with three entanglement distillation protocols from Ref. [27]: double-select (blue solid, 3→1, 3 ops), EXPEDIENT (orange dashed, 5→1, 6 ops), and STRINGENT (green dash-dot, 13→1, 18 ops). Grey-shaded regions indicate the minimum achievable distance at perfect input fidelity ( $F_0 = 100\%$ ), where only local errors contribute. The vertical dashed line in each panel marks the fidelity at which no distillation first achieves a shorter total operation time than every distillation protocol (see Sec. IV A 3); its color matches the last protocol overtaken (double-select, blue). Distance-fidelity model from Eq. (3); error parameters in Table II.

Distillation attempts can be executed either serially or in parallel; detailed analysis of both execution models is provided in Appendix B. As the number of syndrome extraction rounds  $R$  grows large, if successfully distilled pairs can be stored and retrieved across rounds, the long-term average raw consumption per round converges to

$$\lim_{R \rightarrow \infty} \frac{\mathbb{E}[N_{\text{raw}}^{\text{total}}]}{R} = \frac{n_{\text{pairs}}}{p_{\text{succ}}} \times n^{\text{round}}, \quad (10)$$

independently of execution mode. Terminal overhead from unused buffered pairs is negligible for  $R$  large compared to the buffer size. The long-term Bell-pair cost per round is therefore

$$C_{\text{dist}}^{\text{round}} = \frac{n_{\text{pairs}}}{p_{\text{succ}}} \times n^{\text{round}}(p_{\text{eff}}), \quad (11)$$

where  $n^{\text{round}}(p_{\text{eff}}) = ad_s^*(p_{\text{eff}}) - c$  and  $p_{\text{eff}} = f_{\mathcal{D}}(p_{\text{raw}})$ .

We analyze representative protocols with  $n_{\text{pairs}} \in \{1, 3, 5, 13\}$ , corresponding to no distillation and the following entanglement distillation protocols: double selection [27, 28], EXPEDIENT, and STRINGENT [27–29]. These three protocols outperformed other well-known candidates, including BBPSSW [30] and DEJMPS [31], across our parameter regime, and genetic-algorithm searches [27] have not identified a protocol that uniformly surpasses them at all input fidelities. This model assumes Bell pairs remain coherent during storage and that sufficient quantum memory is available for buffering across rounds. Temporal decoherence can degrade buffered Bell pairs and invalidate this assumption; we address memory decay effects in Sec. IV.

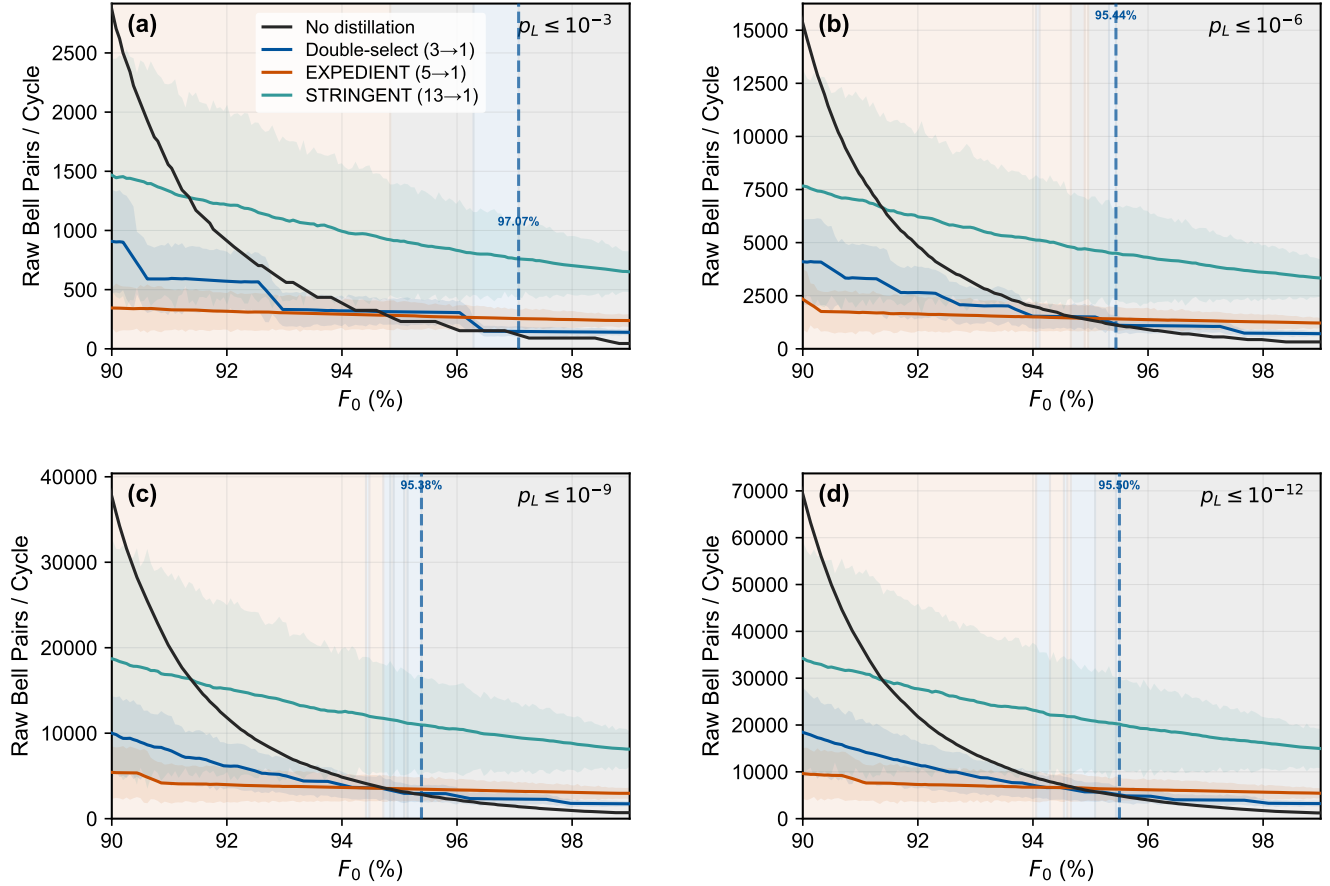


FIG. 4. **Raw Bell-pair consumption per QEC cycle between two logical qubits via remote lattice surgery versus raw Bell-pair fidelity ( $F_0$ ) assuming no decay/decoherence at target logical error rates (a)  $p_L \leq 10^{-3}$ , (b)  $10^{-6}$ , (c)  $10^{-9}$ , (d)  $10^{-12}$ .** Curves compare the no-distillation case (black) with three entanglement distillation protocols from Ref. [27]: double-select 3→1 (blue), EXPEDIENT 5→1 (orange), and STRINGENT 13→1 (green). Cost quantifies total raw Bell-pair consumption, incorporating surface-code distance scaling ( $\propto d_s^2$ ) and distillation overhead. Colored background regions indicate the resource-optimal strategy for different input fidelity regimes. The vertical dashed line marks the fidelity above which no distillation is optimal; its colour (blue) indicates the last protocol overtaken (double-select in all cases). No distillation is optimal for  $F_0 \gtrsim 97.07\%$  (a),  $95.44\%$  (b),  $95.38\%$  (c), and  $95.50\%$  (d). The greatest no-distillation advantage is a 68% overhead reduction ( $F_0 = 98.64\%$ ,  $p_L = 10^{-3}$ : 45 vs 140 pairs/cycle, both  $d_s = 5$ ). Shaded bands show Monte Carlo uncertainty from  $10^3$  runs at 150 fidelity values spanning  $F_0 \in [90.0\%, 99.0\%]$ . Distillation parameters are taken from Ref. [27]; distance–fidelity model is from Eq. (3); error rates are in Table II.

#### D. Distillation optimality criterion

We compare the total Bell-pair consumption of using raw Bell pairs versus entanglement distillation per complete lattice-surgery operation (spanning  $d_s$  syndrome rounds):

$$\begin{aligned} C_{\text{raw}}^{\text{cycle}} &= d_s^*(p_{\text{raw}}) \cdot (ad_s^*(p_{\text{raw}}) - c), \\ C_{\text{dist}}^{\text{cycle}} &= \frac{n_{\text{pairs}}}{p_{\text{succ}}} \cdot d_s^*(p_{\text{eff}}) \cdot (ad_s^*(p_{\text{eff}}) - c), \end{aligned} \quad (12)$$

where  $d_s^*(p_{\text{Bell}})$  denotes the minimum code distance as a function of Bell-pair error rate  $p_{\text{Bell}}$ . Substituting  $d_s^*(p_{\text{eff}}) = \rho d_s^*(p_{\text{raw}})$  from Eq. (9), the cost ratio becomes

$$\frac{C_{\text{dist}}^{\text{cycle}}}{C_{\text{raw}}^{\text{cycle}}} = \frac{n_{\text{pairs}}}{p_{\text{succ}}} \cdot \frac{d_s^*(p_{\text{Bell}})}{d_s^*(p_{\text{raw}})} \frac{[ad_s^*(p_{\text{Bell}}) - c]}{[ad_s^*(p_{\text{raw}}) - c]} \approx \frac{n_{\text{pairs}}}{p_{\text{succ}}} \cdot \rho^2, \quad (13)$$

where the approximation neglects  $c$  relative to  $ad_s^*(p_{\text{raw}})$  and is accurate to within 10% for typical parameters ( $a = 2$ ,  $c = 1$ ,  $d_s \geq 7$ ). Distillation becomes resource-optimal when this ratio falls below unity, i.e., when the quadratic distance reduction ( $\rho^2$ ) more than compensates for the consumption overhead ( $n_{\text{pairs}}/p_{\text{succ}}$ ).

**Direct consumption of raw Bell pairs is resource-optimal when the overhead from entanglement distillation exceeds the benefit from code-distance reduction:**

$$\boxed{\frac{C_{\text{dist}}^{\text{cycle}}}{C_{\text{raw}}^{\text{cycle}}} = \frac{n_{\text{pairs}}}{p_{\text{succ}}} \cdot \rho^2 \gtrsim 1,} \quad (14)$$

where  $\rho$  is the distance ratio (Eq. (9)). Distillation is favored when the quadratic distance gain  $\rho^2$  outweighs the overhead factor  $n_{\text{pairs}}/p_{\text{succ}}$ , i.e., at low fidelities where  $\rho \ll 1$ ; at high fidelities,  $\rho \approx 1$  and the overhead is never justified. Figure 4 confirms this picture across four target logical error rates: the crossover fidelity is remarkably stable at  $F_0 \approx 95\text{--}97\%$  over  $p_L \in [10^{-3}, 10^{-12}]$ , indicating that the optimal strategy is governed primarily by Bell-pair quality rather than the stringency of the target error rate.

#### IV. DISTILLATION TRADE-OFF UNDER TIME-DEPENDENT DECOHERENCE

The preceding analysis assumed Bell pairs are immediately available upon request without decoherence during storage. Under realistic hardware constraints, entanglement generation proceeds at a finite rate determined by the attempt frequency and heralding success probability, while accumulated pairs decohere during waiting periods. This section estimates how these temporal effects modify the distillation trade-off.

##### A. Effects of Stochastic Arrival and Storage Decay

###### 1. Stochastic Bell-pair Generation

When Bell-pair generation proceeds via repeated heralded attempts with success probability  $p_{\text{herald}} \ll 1$ , the sequence of successful events is well-approximated by a Poisson process [17, 32, 33] with rate  $\lambda = I \cdot r_{\text{attempt}} \cdot p_{\text{herald}}$  (Hz), where  $I$  optical interfaces each attempt at rate  $r_{\text{attempt}}$ . The inter-arrival time between consecutive successful generations is exponentially distributed with mean  $1/\lambda$ .

*Collection time statistics.* Collecting  $n^{\text{round}}$  pairs requires waiting through  $n^{\text{round}}$  independent inter-arrival times. The total collection time  $T_{\text{total}}$  follows an Erlang distribution with mean and variance

$$\mathbb{E}[T_{\text{total}}] = \frac{n^{\text{round}}}{\lambda}, \quad \text{Var}[T_{\text{total}}] = \frac{n^{\text{round}}}{\lambda^2}. \quad (15)$$

For sufficiently large  $n^{\text{round}}$ ,  $T_{\text{total}}$  is approximately Gaussian by the central limit theorem. The 99th-percentile collection time is then

$$t_{0.99} = \frac{n^{\text{round}}}{\lambda} \left( 1 + \frac{\Phi^{-1}(0.99)}{\sqrt{n^{\text{round}}}} \right), \quad (16)$$

where  $\Phi^{-1}(0.99) \approx 2.33$  is the 99th percentile of the standard normal distribution. For typical code distances

$d_s \in \{5, 7, 9, 11\}$  ( $n^{\text{round}} \sim 9\text{--}21$ ), the Gaussian approximation error is  $\sim 4\text{--}8\%$ , consistent with the  $O(1/\sqrt{n^{\text{round}}})$  Berry-Esseen bound for the sum of independent and identically distributed exponentials, and sufficient for system-level estimates.

###### 2. Storage Decay

Successfully heralded Bell pairs decohere during storage as

$$F(t) = F_0 e^{-t/\tau_{\text{coh}}}, \quad (17)$$

where  $F_0$  is the initial fidelity and  $\tau_{\text{coh}}$  is the memory coherence time. This is a high-fidelity approximation to the exact depolarizing model  $F(t) = \frac{1}{4} + (F_0 - \frac{1}{4}) e^{-t/\tau_{\text{coh}}}$ , valid when  $F(t) \gg 1/4$ .

Since pairs in a batch arrive at different times, they experience different storage durations before consumption. We impose a *storage cutoff time* [34–36]: any pair is discarded if its storage time would increase its error rate above  $p_{\text{discard}} = 13.3\%$ , chosen slightly below the effective threshold observed in our finite-size simulations,  $p_{\text{th}} \approx 13.36\%$ , whereas the fitted model in Ref. [10] has a Bell-pair error threshold of  $p_{\text{th}} = 15.3\%$ . Evaluating batch quality conservatively via the worst-case (first-generated) pair, the condition  $F_0 e^{-t_{\text{max}}/\tau_{\text{coh}}} \geq F_{\text{discard}}$  yields the maximum viable storage time

$$t_{\text{discard}} = \tau_{\text{coh}} \ln \left( \frac{F_0}{F_{\text{discard}}} \right). \quad (18)$$

###### 3. Time Overhead of Distillation

We compare execution time using circuit depth as a proxy, since two-qubit gates and measurements dominate latency (see Table I in Appendix A). Let  $\tau_{\text{SE}}$  denote the duration of one syndrome extraction round. Here, execution time refers purely to circuit runtime and does not include Bell-pair generation latency or buffering time. Without distillation, a QEC cycle of  $d_s$  rounds costs  $T_{\text{raw}}^{\text{cycle}} = \tau_{\text{SE}} d_{\text{raw}}$ , where  $d_{\text{raw}} \equiv d_s^*(p_{\text{raw}})$ . With distillation, we assume that all purification circuits required for one syndrome round run in parallel, and their execution overlaps with the preceding syndrome extraction round, so only one distillation circuit depth  $\tau_{\text{D}}$  is added per round, giving

$$T_{\text{dist}}^{\text{cycle}} = (\tau_{\text{D}} + \tau_{\text{SE}}) d_{\text{dist}}, \quad d_{\text{dist}} \equiv d_s^*(p_{\text{eff}}). \quad (19)$$

Distillation reduces total execution time when  $T_{\text{dist}}^{\text{cycle}} < T_{\text{raw}}^{\text{cycle}}$ , i.e.,  $(\tau_{\text{D}} + \tau_{\text{SE}}) d_{\text{dist}} < \tau_{\text{SE}} d_{\text{raw}}$ , which rearranges to

$$\frac{d_{\text{dist}}}{d_{\text{raw}}} < \frac{1}{1 + \tau_{\text{D}}/\tau_{\text{SE}}}. \quad (20)$$

For STRINGENT, which has the largest circuit depth among the protocols considered ( $\approx 18$  timesteps  $\approx 3.75 \tau_{\text{SE}}$ ), this threshold corresponds to  $d_{\text{dist}}/d_{\text{raw}} \lesssim 0.21$ . In the low-fidelity regime where  $d_{\text{dist}} \ll d_{\text{raw}}$ , Eq. (20) is easily satisfied and distillation reduces  $T$  substantially. As raw fidelity increases and  $d_{\text{dist}}/d_{\text{raw}} \rightarrow 1$ , the condition is violated and distillation becomes slower than direct use. Although the focus here is on execution time, Bell-pair consumption  $N_{\text{QEC}}$  follows a steeper  $d^2$  scaling (Eq. (14)): the time crossover therefore generally occurs at a comparable or slightly lower fidelity than the Bell-pair crossover, though the gap depends on  $\tau_{\text{D}}/\tau_{\text{SE}}$  and closes as this ratio decreases. Fig. 3 shows the fidelity above which the no-distillation protocol achieves shorter execution time than every distillation protocol (Eq. (20)); Fig. 4 shows the corresponding crossover in raw Bell-pair consumption per QEC cycle, where the no-distillation cost (Eq. (14)) is compared against that of the best-performing distillation protocol at each fidelity point. As an example, at  $p_L \leq 10^{-3}$ , the time crossover occurs at  $F_0 \approx 97.04\%$  while the Bell-pair consumption crossover occurs at  $F_0 \approx 97.07\%$ .

## B. Rate-Limited Operating Regimes

We denote the protocol-dependent round duration by  $T^{\text{round}}$ , with  $T^{\text{round}} \in \{T_{\text{raw}}^{\text{round}}, T_{\text{dist}}^{\text{round}}\}$ , where  $T_{\text{raw}}^{\text{round}} = \tau_{\text{SE}}$  in the absence of distillation and  $T_{\text{dist}}^{\text{round}} = \tau_{\text{D}} + \tau_{\text{SE}}$  when distillation is employed (Sec. IV A 3).

We similarly denote the protocol-dependent per-round Bell-pair consumption by  $C^{\text{round}} \in \{C_{\text{raw}}^{\text{round}}, C_{\text{dist}}^{\text{round}}\}$ , with  $C_{\text{raw}}^{\text{round}} = n^{\text{round}}$  and  $C_{\text{dist}}^{\text{round}} = \frac{n_{\text{pairs}}}{p_{\text{succ}}} n^{\text{round}}$ , where  $n^{\text{round}} = ad_s - c$  (Eqs. (1), (11)).

The operating regime is determined by comparing the expected number of Bell pairs generated per round,  $n_{\text{gen}} \equiv \lambda T^{\text{round}}$ , to the per-round consumption  $C^{\text{round}}$ .

### 1. On-the-fly Operation

The related question of when to distill, including whether to process pairs as they arrive or to batch them, is studied in Ref. [37]. Here we assume all raw pairs for one round are available at the start of the round.

When entanglement generation keeps pace with consumption within each round, the *on-the-fly* condition (OTF) reads

$$\lambda T^{\text{round}} - \Phi^{-1}(0.99)\sqrt{\lambda T^{\text{round}}} \geq C^{\text{round}}. \quad (21)$$

In the on-the-fly regime, the worst-case storage time is  $t_{\text{max}} \lesssim T^{\text{round}}$ . We denote by  $F_{\text{stored}}$  the fidelity of a Bell pair after storage decay, i.e. Eq. (17) evaluated at the worst-case wait time. This gives

$$F_{\text{stored}} \geq F_0 e^{-T^{\text{round}}/\tau_{\text{coh}}} \approx F_0 \left(1 - \frac{T^{\text{round}}}{\tau_{\text{coh}}}\right). \quad (22)$$

The raw input pairs for distillation are stored for a longer time, experiencing up to  $T_{\text{dist}}^{\text{round}}/T_{\text{raw}}^{\text{round}}$  times the exposure duration compared to pairs consumed directly without distillation (Eq. (19)). For the protocols considered in this work,  $T_{\text{dist}}^{\text{round}} \lesssim 6 T_{\text{raw}}^{\text{round}}$ . However, distillation suppresses input errors to second order ( $p_{\text{eff}} \sim p_{\text{raw}}^2$ ), so a perturbation  $\delta p_{\text{raw}}$  propagates as  $\delta p_{\text{eff}} \approx 2 p_{\text{raw}} \delta p_{\text{raw}}$ . Near the crossover ( $p_{\text{raw}} \approx 5\text{--}10\%$ ), the factor  $2 p_{\text{raw}} \approx 0.1\text{--}0.2$  strongly attenuates the effect of the  $\sim 6\times$  longer storage time in the distillation case. As a result, both approaches acquire comparable additional error of order  $\nu \equiv T^{\text{round}}/\tau_{\text{coh}}$  per syndrome cycle. Equivalently, the effective operating fidelity of each shifts from  $F_0$  to  $F_0 - O(\nu)$ . Because this is largely a common-mode shift, the crossover fidelity is only weakly affected by storage decoherence.

### 2. No-expire Regime

When  $\lambda < n^{\text{round}}/T^{\text{round}}$  but the link efficiency  $\eta_{\text{link}} \equiv \lambda \tau_{\text{coh}}$  is large enough that the earliest pair has not decayed below  $F_{\text{th}}$  by the time all  $N_{\text{QEC}}$  pairs are collected, the system operates in the no-expire regime. The full batch arrives slower than one syndrome cycle, so the surface-code patch idles while waiting for collection to complete; yet no pair is discarded.

Two scheduling strategies can accommodate this regime (Fig. 5(b)): *round-by-round*, which feeds pairs to the code as each syndrome round becomes ready, and *pre-buffered*, which accumulates all  $N_{\text{QEC}}$  pairs before starting extraction. A detailed comparison in Appendix C shows that the round-by-round strategy (Strategy 1) dominates: it limits storage to at most one round's worth of pairs, whereas batch collection forces the earliest pair to wait for the full accumulation time. We therefore adopt Strategy 1 throughout.

Under Strategy 1, the earliest pair in each round decays to

$$F_{\text{stored}} \approx F_0 e^{-C^{\text{round}}/\eta_{\text{link}}}, \quad (23)$$

This fidelity degradation increases the required code distance; the resulting self-consistency condition and the minimum  $\eta_{\text{link}}$  it implies are derived in the next section.

To quantify how finite generation rate and memory decoherence reshape the distillation trade-off, we solve the self-consistent distance equation (Eq. (C3)) over a range of fidelities  $F_0 = 90\text{--}99\%$  at several representative  $(p_L, \lambda)$  settings (Fig. 6). Two decoherence time scales govern the penalty:  $\tau_{\text{coh}}$ , which controls how quickly stored Bell pairs depolarise toward the maximally mixed state, and  $\tau_{\text{dep}} = \mu \tau_{\text{coh}}$ , which sets the rate at which idling data qubits accumulate errors between syndrome rounds. The ratio  $\mu \equiv \tau_{\text{dep}}/\tau_{\text{coh}}$  is a platform-dependent parameter satisfying  $\mu \geq 1$ : a stored Bell pair is distributed across two nodes whose qubits decohere independently, so its fidelity generically decays faster than that of a single data qubit. We adopt  $\tau_{\text{coh}} = 10\text{ s}$ ,  $\mu = 5$ ,

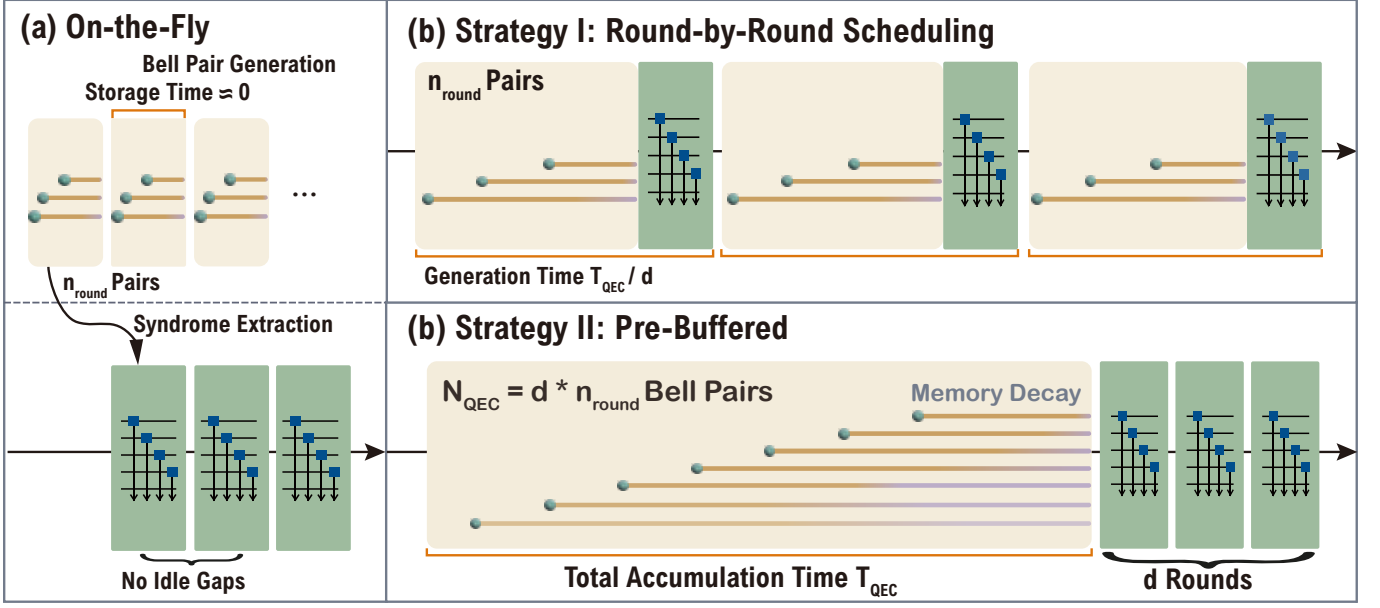


FIG. 5. Bell-pair scheduling schemes for remote lattice surgery above and below the on-the-fly threshold  $\lambda_{\text{th}}$  (Eq. (21)). (a) On-the-fly regime ( $\lambda \geq \lambda_{\text{th}}$ ): the generation rate is sufficient to supply each syndrome round on demand, so Bell pairs are consumed immediately with worst-case storage time bounded by  $T^{\text{round}}$  (Eq. (22)). (b) Below threshold ( $\lambda < \lambda_{\text{th}}$ ), two strategies arise. *Strategy 1* (round-by-round): because generation cannot keep pace, collecting  $n^{\text{round}}$  pairs per round requires a finite accumulation window; pairs generated early in the window must wait in memory until the round begins, degrading their fidelity (Eq. (23)), and data qubits likewise accumulate idle error during the wait (Eq. (C2)). *Strategy 2* (pre-buffered): all  $N_{\text{QEC}}$  pairs are collected before any syndrome extraction begins; the  $\tilde{d}_s$  rounds then proceed back to back, eliminating data-qubit idle error but exposing the earliest pairs to decay over the full accumulation time  $T_{\text{QEC}}$  (Eq. (C4)). In both strategies the required code distance  $\tilde{d}_s$  and the per-round consumption  $n^{\text{round}}$  are mutually dependent, necessitating the self-consistent iteration of Eq. (C3) (Algorithm 1).

and  $\tau_{\text{SE}} = 1 \text{ ms}$  [8] as conservative baselines and examine sensitivity to  $\mu$  in Fig. 7. At the generation rates considered ( $\lambda = 5\text{--}100 \text{ kHz}$ ), this gives link efficiencies  $\eta_{\text{link}} = 5 \times 10^4\text{--}10^6$  (Eq. (21)), spanning the no-expire through on-the-fly regimes. Because all decoherence enters through  $\eta_{\text{link}}$ , the results scale directly with memory lifetime: longer  $\tau_{\text{coh}}$  widens the no-expire window and shrinks the idle penalty, while shorter  $\tau_{\text{coh}}$  pushes the system towards infeasibility. The ratio  $\mu$  modulates only the data-qubit idle error (Eq. (C2)); increasing it suppresses the gap between the static and no-expire cost curves, whereas  $\mu \rightarrow 1$  amplifies the penalty and narrows the feasible region.

Figure 6 compares the static (solid) and converged Strategy 1 (dashed) costs across four  $(\lambda, p_L)$  settings. In the OTF zone (panels b, d) the cost tracks the static prediction; the crossover analysis of Sec. III D applies directly. In the no-expire regime the self-consistency loop (C3) inflates  $\tilde{d}_s$ , opening the shaded gap between the two curves. Because  $C^{\text{round}} = (n_{\text{pairs}}/p_{\text{succ}}) \times n^{\text{round}}(\tilde{d}_s)$ , the feedback gain is amplified by  $n_{\text{pairs}}/p_{\text{succ}}$ : raw Bell pairs ( $n_{\text{pairs}} = 1$ ) have the weakest feedback, while STRINGENT (13 : 1) has the strongest and is the first to become infeasible. Because temporal decoherence penalises distillation more heavily than no-distillation, the

crossover fidelity generically shifts downward (toward lower  $F_0$ ) or disappears altogether. At low  $\lambda$  (panel a) this effect is most pronounced: the amplified feedback inflates  $\tilde{d}_s^{\text{dist}}$  toward  $\tilde{d}_s^{\text{raw}}$ , eroding the advantage  $\rho^2$  (Eq. (13)). Once the converged ratio  $\tilde{\rho} \equiv \tilde{d}_s^{\text{dist}}/\tilde{d}_s^{\text{raw}}$  satisfies  $(n_{\text{pairs}}/p_{\text{succ}})\tilde{\rho}^2 > 1$  across the entire feasible  $F_0$  range, no-distillation is everywhere cheaper and the static crossover vanishes. Conversely, increasing  $\lambda$  shrinks the collection window  $C^{\text{round}}/\lambda$ ; as  $\eta_{\text{link}} \rightarrow \infty$  the dashed curves collapse onto the solid ones, recovering the static limit. The static cost ranking is therefore a conservative guide for protocol selection: whenever it favours no-distillation, the decoherence analysis under Strategy 1 confirms or strengthens that conclusion.

### 3. Minimum Link Efficiency Threshold

For a given  $\tau_{\text{coh}}$ , achieving  $p_L^{\text{target}}$  requires a minimum link efficiency set by a self-consistency condition. During collection of one round's Bell pairs, the earliest pair decays to  $F_{\text{stored}} \approx F_0 e^{-C^{\text{round}}/\eta_{\text{link}}}$  (Eq. (23)), where  $C^{\text{round}}$  is the per-round raw consumption (Eqs. (1), (11)). This degradation increases the code distance needed to meet  $p_L^{\text{target}}$ , which increases  $C^{\text{round}}$ , which lengthens col-

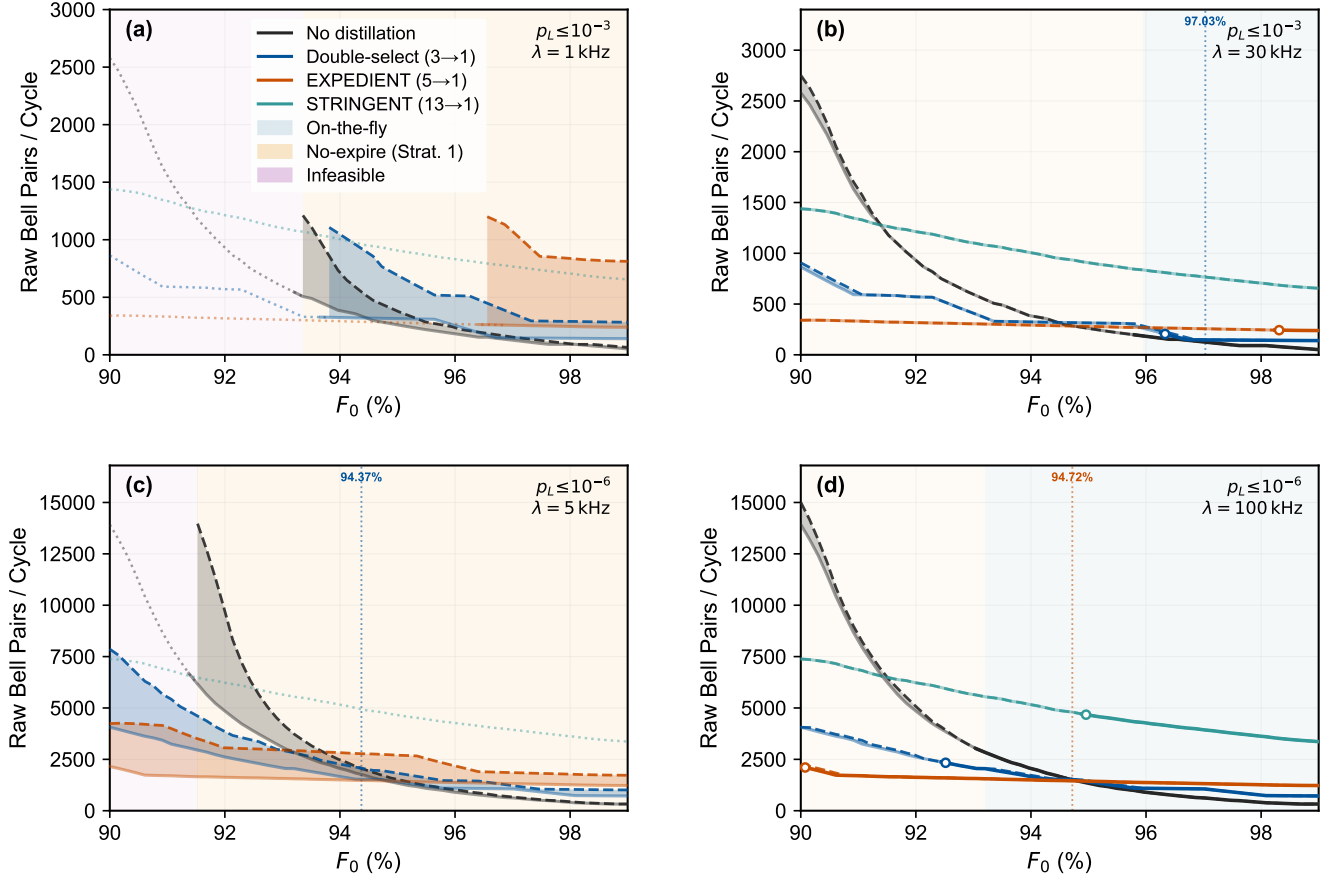


FIG. 6. **Operating-regime classification for the no-distillation protocol at four representative  $(p_L, \lambda)$  settings.** Fixed parameters:  $\tau_{SE} = 1$  ms,  $\tau_{coh} = 10$  s,  $\tau_{dep} = 50$  s ( $\mu = 5$ ). Background shading marks the no-distillation regime boundaries: *on-the-fly* (green, Eq. (21)), *no-expire* (yellow, Eq. (C3)), and *infeasible* (pink). Solid lines show the static (no-decay) cost: full opacity in the on-the-fly zone, reduced opacity in the no-expire zone, and dotted in infeasible regions; an open circle marks the OTF / no-expire transition for each distillation protocol. Dashed lines show the converged no-expire cost, in which both Bell-pair decay and data-qubit idle depolarisation (Eq. (C2)) feed back into  $\tilde{d}_s$ ; the shaded fill between solid and dashed curves visualises the resulting cost overhead. Panel (a): at  $\lambda = 1$  kHz, no-distillation is the cheapest protocol across the entire feasible  $F_0$  range. Panels (a)–(b): raising  $\lambda$  from 1 to 30 kHz eliminates the infeasible zone and opens the OTF regime at moderate  $p_L$ ; panels (c)–(d): at the stricter target  $p_L \leq 10^{-6}$ , raising  $\lambda$  from 5 to 100 kHz likewise removes infeasibility and enables on-the-fly operation.

lection and causes further decay.

The self-consistent code distance  $\tilde{d}_s$  satisfies, without distillation,

$$\tilde{d}_s = d_s^* \left( 1 - F_0 e^{-(a\tilde{d}_s - c)/\eta_{\text{link}}}, p_L^{\text{target}} \right), \quad (24)$$

and with distillation,

$$\tilde{d}_s = d_s^* \left( f_{\mathcal{D}} \left( 1 - F_0 e^{-C_{\text{dist}}^{\text{round}}(\tilde{d}_s)/\eta_{\text{link}}} \right), p_L^{\text{target}} \right). \quad (25)$$

Starting from the static estimate  $d_s^{(0)} = d_s^*(p_{\text{raw}}, p_L^{\text{target}})$  (Eq. (4)), each iteration computes the decay-degraded fidelity at the current  $\tilde{d}_s$  and updates the required distance. Above a critical  $\eta_{\text{link}}^{\text{min}}(F_0, p_L^{\text{target}})$ , the iteration converges to a finite  $\tilde{d}_s \geq d_s^{(0)}$ . Below it, each iteration produces a strictly larger distance, and no finite solution exists: the target  $p_L^{\text{target}}$  is unachievable regardless

of scheduling strategy. We emphasize that this iterative procedure is performed at design time. It determines the code distance that must be chosen before the lattice-surgery operation begins, given the expected decoherence during Bell-pair collection. It does not correspond to a physical, real-time expansion of the surface-code patch.

Equivalently, the converged solution defines a discard fidelity  $F_{\text{discard}}(\tilde{d}_s, p_L^{\text{target}})$ , the lowest fidelity at which  $\tilde{d}_s$  still achieves  $p_L^{\text{target}}$ . The self-consistent bound then takes the form of a production constraint at this fidelity,

$$\eta_{\text{link}} \geq \frac{C^{\text{round}}(\tilde{d}_s)}{\ln(F_0/F_{\text{discard}})} \left( 1 + \frac{\Phi^{-1}(0.99)}{\sqrt{C^{\text{round}}(\tilde{d}_s)}} \right). \quad (26)$$

A narrow marginal regime exists below this bound where operation remains possible through over-generation:

early pairs expire and are replaced within a sliding window of width  $t_{\text{discard}}$ , at the cost of higher memory occupancy.

The distinction from a naive production bound is that both  $\tilde{d}_s$  and  $F_{\text{discard}}$  are determined self-consistently: a lower  $F_{\text{discard}}$  permits more decay but demands a larger  $\tilde{d}_s$ , which increases  $C^{\text{round}}$  and tightens the bound.

## V. INTEGRATED FEASIBILITY CRITERIA AND PLATFORM ASSESSMENT

We briefly consider the feasibility of our methods in the context of current and next-generation neutral atom and ion trap quantum computers. A more detailed analysis requires a complete description of the intra-module architectures.

*Trapped ions.* We analyze which operating regime is accessible for state-of-the-art trapped-ion systems. The highest demonstrated remote Bell-pair fidelity  $F_0 = 97.0\%$  [21], achieved via time-bin photonic encoding, falls comfortably within the no-distillation regime identified in Sec. III D, where direct consumption of raw Bell pairs is resource-optimal, but at a very limited generation rate of  $\lambda = 0.35 \text{ s}^{-1}$ . The highest demonstrated entanglement generation rate  $\lambda = 250 \text{ s}^{-1}$  [32], achieved via polarization encoding at  $F_0 = 94\%$ , represents a substantially higher rate, yet still falls short of the on-the-fly threshold by roughly two orders of magnitude even at the relatively modest target of  $p_L = 10^{-3}$ , assuming a conservative  $\tau_{\text{SE}} = 1 \text{ ms}$  [8], placing current trapped-ion systems in the no-expire regime. Note that the high-rate and high-fidelity results stem from different experiments employing distinct photonic encodings. Reaching the on-the-fly regime will likely require spatial multiplexing of photonic interfaces, where deploying  $I > 1$  parallel optical channels per module scales  $\lambda$  linearly with  $I$ .

Currently, entanglement stored on a memory qubit retains a fidelity of 0.81 after 10 s [38], corresponding to  $\tau_{\text{coh}} \approx 65 \text{ s}$  via Eq. (17), giving  $\eta_{\text{link}} = \lambda \tau_{\text{coh}} \approx 1.6 \times 10^4$ . While fundamental single-ion memories have demonstrated coherence times exceeding 5500 s [39], bridging this gap in network operations would theoretically project  $\eta_{\text{link}}$  to the order of  $10^6$ .

The binding constraint is processor capacity (see Appendix D): a single  $d_s = 5$  logical qubit requires  $2d_s^2 - 1 = 49$  physical qubits. The quantum charge-coupled device (QCCD) architecture [40] is a promising platform for intra-module scaling, with state-of-the-art processors recently reaching 98 physical qubits [41]. It is worth noting, however, that demonstrations encoding up to 48 logical qubits on such hardware, while resource-efficient, rely on high-rate codes whose error-detection-only schemes do not scale efficiently to arbitrarily large circuits. Furthermore, their reliance on dense intra-block connectivity poses significant challenges for extension to distributed architectures. Therefore, supporting a larger number of robust logical qubits necessitates a transition toward

multi-module distributed computation, which serves as the primary motivation for the inter-module architecture explored in this study.

*Neutral atoms.* Atom-photon entanglement in neutral-atom systems has progressed steadily over the past two decades. For single-node atom-photon entanglement, the highest reported raw fidelity is  $F_0 = 0.952$  using free-space polarization-encoded collection [42], while cavity-enhanced collection has achieved a single-attempt success probability of 0.33 at  $F_0 = 0.866(50)$  [43]. Most recently, a compact parabolic-mirror node reached  $F_0 = 0.93$  with a per-attempt success probability of 0.022 [44], and telecom-wavelength time-bin encoding with  $^{171}\text{Yb}$  yielded  $F_0 = 0.90(1)$  [45].

For two-node atom-atom remote entanglement, heralded Bell pairs have been distributed over a 400m line-of-sight link (700m fibre) at  $F_0 \geq 0.892(23)$  [42], with heralding rates of order  $10^{-2} \text{ s}^{-1}$ , still several orders of magnitude below the on-the-fly threshold. Projected cavity-enhanced schemes with  $\lambda \sim 10^5 \text{ s}^{-1}$  at  $F_0 \approx 0.999$  [46], combined with the observed  $\tau_{\text{coh}} \sim 10 \text{ s}$ -scale hyperfine coherence [47], would yield  $\eta_{\text{link}} \gtrsim 10^6$ , placing neutral-atom links well within the on-the-fly correction regime. At the same time, recent experiments have demonstrated that neutral-atom network nodes support strong spatial and register-based multiplexing, enabling single nodes to achieve substantially enhanced entanglement generation rates that scale with the number of emitters [43, 45].

The potential advantage over trapped ions is module capacity: arrays of several hundred physical qubits [47, 48] relax the processor-size constraint that limits current ion-trap modules.

## VI. CONCLUSION

We have analyzed the resource trade-off between distillation-free and distillation-assisted remote lattice surgery for the rotated surface code under both static and time-dependent noise models. Three principal findings emerge.

First, we derive an explicit condition (Eq. (14)) for choosing between direct and distillation-assisted consumption of Bell pairs: distillation-free operation is resource-optimal when the quadratic distance saving from purification no longer compensates for the per-pair overhead. Under a static model with no memory decoherence, this crossover occurs at  $F_0 \approx 95\%$ , is stable across  $p_L \in [10^{-3}, 10^{-12}]$ , and yields overhead reductions up to 68% ( $F_0 \approx 98.64\%$ ,  $p_L = 10^{-3}$ ).

Second, incorporating finite generation rates and memory decoherence, we identify three operating regimes: on-the-fly, where generation keeps pace with each syndrome round; no-expire, where pairs arrive slower and must wait in memory, but their fidelity remains usable by the time they are consumed; and infeasible, where decoherence outpaces any achievable code distance. In the no-expire

regime, Bell-pair decay and data-qubit idle errors feed back into the required code distance via a self-consistency condition (Eq. (C3)), inflating costs beyond the static estimate. Nonetheless, where distillation-free operation is already favored under the static model, this conclusion remains robust under temporal decoherence.

Third, current trapped-ion links ( $F_0 = 97\%$  [21],  $\lambda = 250\text{ s}^{-1}$  [32]) already fall within the distillation-free regime but operate in the no-expire window, while projected cavity-enhanced neutral-atom links ( $\lambda \sim 10^5\text{ s}^{-1}$ ,  $F_0 \approx 0.999$  [46]) would reach the on-the-fly regime. These two platforms are representative of the parameter space analyzed here and provide concrete co-design targets for photonic interconnects, memory lifetimes, and fault-tolerant logical layouts. An alternative approach is transversal gate teleportation, discussed in Appendix E.

Several natural extensions of this analysis remain for future work. The scheduling analysis in this work focuses on single lattice surgery operations and does not exploit idle periods between remote operations for pre-generating Bell pairs; accounting for algorithm-level scheduling and inter-module connectivity patterns could further reduce resource costs. The framework presented here is hardware-agnostic, but it can be combined with platform-specific parameters to provide a foundation for systematic architectural design; a detailed resource analysis along these lines will be presented in forthcoming work. Finally, this study assumes a uniform code distance throughout the architecture; allowing different distances for data, routing, and communication patches may further reduce the physical qubit overhead.

## ACKNOWLEDGMENTS

The authors are grateful to Frank Mueller, Pedro Lopes, and Abhinav Anand for helpful discussions. Sitong Liu acknowledges support from the National Science Foundation STAQ project under Grant No. PHY-2325080. This research used resources of the National Energy Research Scientific Computing Center, a DOE Office of Science User Facility supported by the Office of Science of the U.S. Department of Energy under Contract No. DE-AC02-05CH11231 using NERSC award ASCR-ERCAP0037552. This work was also supported in part by the U.S. Department of Energy, Office of Science, under Award No. DE-SCL0000039 to Lawrence Berkeley National Laboratory (PI: Erhan Saglamyurek). Numerical simulations used the `qevo` package (<https://github.com/Krastanov/qevo>) for optimized entanglement distillation protocols, and Stim [49] and PyMatching for circuit-level noise simulation and decoding. This work was initiated and primarily led by the first author, based on research conducted at Lawrence Berkeley National Laboratory in the summer of 2025.

## DATA AVAILABILITY

The numerical data underlying all figures are available at <https://github.com/sitong1011/remotels> and will be made public upon publication.

## CODE AVAILABILITY

All resource estimates and regime boundaries are derived from the analytical framework presented in this work. The Stim circuit definitions and PyMatching decoding scripts used for the lattice-surgery simulations (Appendix C) are available at <https://github.com/sitong1011/remotels> and will be made public upon publication.

## Appendix A: Model parameters

We summarize the time-scale hierarchy and noise model parameters used throughout this work in Tables I and II, respectively.

TABLE I. Time-scale hierarchy in distributed QEC.

Time scale	Symbol	Typical value
Two-qubit gate	$t_{\text{gate}}$	1 (reference)
Measurement	$t_{\text{meas}}$	$\sim t_{\text{gate}}$
Syndrome extraction	$\tau_{\text{SE}}$	$\sim 5 t_{\text{gate}}$
Distillation circuit	$\tau_{\text{D}}$	$4\text{--}24 t_{\text{gate}}$
Memory coherence	$\tau_{\text{coh}}$	$\gg \tau_{\text{SE}}$
Data-qubit depolarising	$\tau_{\text{dep}}$	$\mu \tau_{\text{coh}}$

## Appendix B: Distillation execution models

### 1. Serial Execution with Restarts

If distillation attempts are executed sequentially until success, the expected number of attempts required to obtain one purified pair is  $1/p_{\text{succ}}$ . The expected raw Bell-pair cost per syndrome extraction round is therefore

$$\mathbb{E}[N_{\text{raw}}^{(\text{serial})}] = \frac{n_{\text{pairs}}}{p_{\text{succ}}} \cdot n^{\text{round}}(p_{\text{eff}}), \quad (\text{B1})$$

where each distillation attempt consumes  $n_{\text{pairs}}$  raw pairs with success probability  $p_{\text{succ}}$ , and each syndrome extraction round requires  $n^{\text{round}}(p_{\text{eff}})$  distilled pairs at error rate  $p_{\text{eff}}$ .

In the most conservative restart structure, any measurement failure contaminates the target Bell pair and forces a complete restart of the protocol, so that all raw Bell pairs used in the failed attempt are discarded. This *full-restart* behavior is exemplified by double-selection

TABLE II. **Noise model parameters for local and non-local operations in distillation protocols and lattice surgery** (see Fig. 4 and Fig. 3). Local error rate  $p_{\text{local}} = 0.1\%$  adopted from Sunami *et al.* [10]. Single-qubit idle errors are included only in the circuit-level simulations of Appendix. C.

Operation	Noise model	Error rate
<b>Local operations</b>		
Single-qubit gates	Depolarizing: uniform Pauli error over $\{X, Y, Z\}$ , each $p_{\text{local}}/3$	$p_{\text{local}} = 0.1\%$
Two-qubit gates	Two-qubit depolarizing: uniform over 15 non-identity Paulis, each $p_{\text{local}}/15$	$p_{\text{local}} = 0.1\%$
Measurement / Reset	Bit-flip or phase-flip	$p_{\text{local}} = 0.1\%$
Idle (no-expire regime only)	Depolarizing: uniform Pauli error over $\{X, Y, Z\}$ , each $p_{\text{idle}}/3$	$p_{\text{idle}}$ (Eq. C2)
<b>Non-local operations</b>		
Bell-pair preparation	Two-qubit depolarizing on distributed Bell state	$p_{\text{Bell}}$ (Eq. 17)

purification [28], where  $n_{\text{pairs}} = 3$  and a failure at either selection step requires restarting the entire circuit.

More generally, some distillation circuits admit selective-retry structures, in which only the failed sub-circuits and their dependent operations must be re-executed. Such protocols reduce the expected raw Bell-pair consumption relative to the full-restart case at fixed  $p_{\text{succ}}$ . In either case, Eq. (B1) provides the baseline against which parallel execution is compared.

## 2. Parallel Execution

To achieve  $\geq 99\%$  success probability per syndrome extraction round, we execute  $k$  independent distillation attempts in parallel, where

$$k = \left\lceil \frac{\log(0.01)}{\log(1 - p_{\text{succ}})} \right\rceil, \quad (\text{B2})$$

ensures  $1 - (1 - p_{\text{succ}})^k \geq 0.99$  [8]. The total raw Bell-pair cost per syndrome extraction round is then

$$C^{\text{round}} = n^{\text{round}} \times n_{\text{pairs}} \times k, \quad (\text{B3})$$

where  $n^{\text{round}} = ad_s^*(p_{\text{eff}}) - c$  is the number of purified pairs required per syndrome extraction round,  $n_{\text{pairs}}$  is the raw input consumption per distillation attempt, and  $k$  is the multiplexing factor that ensures  $\geq 99\%$  success probability per round.

If successfully distilled Bell pairs can be buffered across rounds, the long-term average consumption converges to the serial rate: each batch of  $k$  parallel attempts yields an expected  $k \cdot p_{\text{succ}}$  successes while consuming  $k \cdot n_{\text{pairs}}$  raw pairs, giving a cost per success of  $n_{\text{pairs}}/p_{\text{succ}}$ , identical to Eq. (B1).

## Appendix C: Detailed Comparison of Scheduling Strategies

A critical bottleneck in remote lattice surgery arises when the entanglement generation rate  $\lambda$  cannot sustain continuous lattice surgery operations, i.e., when

$\lambda < n^{\text{round}}/T^{\text{round}}$  (Sec. IV B). The system must then absorb unavoidable idle time, introducing a fundamental scheduling dilemma [50]. Accumulating all  $N_{\text{QEC}}$  pairs before surgery exposes early pairs to severe memory decay, whereas executing surgery round-by-round with intermediate pauses leaves the coupled data qubits subject to uncorrected idle errors. We analyze two concrete strategies that represent these extremes.

### 1. Strategy 1: Round-by-round Scheduling

Generate  $n^{\text{round}} = ad_s - c$  Bell pairs per syndrome round, then immediately execute one round of syndrome extraction with teleported CNOTs along the seam. Because  $\lambda < n^{\text{round}}/T^{\text{round}}$ , both patches idle with the noisy seam coupled while awaiting the next batch, and the cycle repeats across  $d_s - 1$  rounds. Neglecting stochastic fluctuations in the Poisson arrival times (see Eq. (16)), the earliest pair in each batch waits approximately  $n^{\text{round}}/\lambda$  and decays to

$$F_{\text{stored}}^{\text{S1}} \approx F_0 \exp\left(-\frac{n^{\text{round}}}{\eta_{\text{link}}}\right), \quad (\text{C1})$$

giving  $p_{\text{Bell}}^{\text{S1}} = 1 - F_{\text{stored}}^{\text{S1}}$ . Between rounds, data qubits wait  $\Delta t_{\text{idle}} \approx n^{\text{round}}/\lambda$  with the seam coupled but inactive. Modeling this wait as symmetric depolarizing noise with characteristic time  $\tau_{\text{dep}} = \mu \tau_{\text{coh}}$ , the per-round idle error applied to every data qubit is

$$p_{\text{idle}} = 1 - \exp\left(-\frac{n^{\text{round}}}{\mu \eta_{\text{link}}}\right), \quad \mu \equiv \tau_{\text{dep}}/\tau_{\text{coh}}, \quad (\text{C2})$$

where  $\mu \geq 1$  is the ratio of the data-qubit memory lifetime to the Bell-pair coherence time. When  $\mu \gg 1$  the idle penalty is negligible and Strategy 1 dominates; as  $\mu \rightarrow 1$  the idle cost grows and Strategy 2 becomes competitive. This error is injected before each of the  $d_s - 1$  syndrome rounds that follow the initial merge round, so the effective local error rate entering the decoder is  $\tilde{p}_{\text{local}} \simeq p_{\text{phys}} + p_{\text{idle}}$  (neglecting the  $O(p^2)$  cross-term), where  $p_{\text{phys}}$  is the local error rate from all non-idle sources (Table II).

The effective Bell-pair error  $p_{\text{Bell}}$  and idle-induced local error  $\tilde{p}_{\text{local}}$  both depend on  $d_s$  through  $n^{\text{round}} = ad_s - c$

(Eq. (1)), while  $\tilde{d}_s$  is itself determined by these error rates via Eq. (4). This defines a self-consistency condition analogous to Eqs. (24)–(25), which we solve via the iterative procedure in Algorithm 1:

$$\tilde{d}_s = d_s^* \left( p_{\text{Bell}}(\tilde{d}_s), \tilde{p}_{\text{local}}(\tilde{d}_s) \right), \quad (\text{C3})$$

where  $p_{\text{Bell}}(\tilde{d}_s) = 1 - F_{\text{stored}}^{\text{S1}}$  and  $\tilde{p}_{\text{local}}(\tilde{d}_s) = p_{\text{phys}} + p_{\text{idle}}$  (Eq. (C2)).

## 2. Strategy 2: Pre-buffered

Accumulate all  $N_{\text{QEC}} = \tilde{d}_s n^{\text{round}}$  pairs while both patches run independent local QEC cycles with no seam coupling, then execute all  $\tilde{d}_s$  rounds back-to-back. Because the patches are decoupled throughout accumulation, we assume  $\tilde{p}_{\text{local}}^{\text{S2}} = p_{\text{phys}}$  with no idle penalty. However, the earliest pair waits  $\tilde{d}_s$  times longer than in Strategy 1 and decays to

$$F_{\text{stored}}^{\text{S2}} \approx F_0 \exp\left(-\frac{\tilde{d}_s n^{\text{round}}}{\eta_{\text{link}}}\right), \quad (\text{C4})$$

yielding  $p_{\text{Bell}}^{\text{S2}} \gg p_{\text{Bell}}^{\text{S1}}$  (Eqs. (23), (C4)).

---

### Algorithm 1 Self-consistent distance solver.

Strategy 1 (round-by-round) and Strategy 2 (pre-buffered).

---

**Require:**  $\lambda, \tau_{\text{coh}}, \mu, F_0, p_{\text{phys}}, \tau_{\text{SE}}, p_L^{\text{target}}, d_{\text{max}}, \text{strategy} \in \{1, 2\}$

**Ensure:**  $\tilde{d}_s$  or INFEASIBLE

```

1:  $\eta_{\text{link}} \leftarrow \lambda \tau_{\text{coh}}$ 
2:  $\tilde{d}_s \leftarrow d_s^*(p_{\text{raw}}, p_{\text{phys}}, p_L^{\text{target}})$   $\triangleright$  Eq. (4)
3: loop
4:    $n \leftarrow a \tilde{d}_s - c$   $\triangleright$  Eq. (1)
5:   if strategy = 1 then
6:      $F_{\text{stored}} \leftarrow F_0 e^{-n/\eta_{\text{link}}}$   $\triangleright$  Eq. (23)
7:      $p_{\text{idle}} \leftarrow 1 - e^{-n/(\mu \eta_{\text{link}})}$   $\triangleright$  Eq. (C2)
8:   else
9:      $F_{\text{stored}} \leftarrow F_0 e^{-\tilde{d}_s n/\eta_{\text{link}}}$   $\triangleright$  Eq. (C4)
10:     $p_{\text{idle}} \leftarrow 0$ 
11:  end if
12:   $\tilde{d}_s' \leftarrow d_s^*(1 - F_{\text{stored}}, p_{\text{phys}} + p_{\text{idle}}, p_L^{\text{target}})$   $\triangleright$ 
     $\tilde{p}_{\text{local}} = p_{\text{phys}} + p_{\text{idle}}$ 
13:  if  $\tilde{d}_s' > d_{\text{max}}$  then return INFEASIBLE
14:  end if
15:  if  $\tilde{d}_s' = \tilde{d}_s$  then return  $\tilde{d}_s$ 
16:  end if
17:   $\tilde{d}_s \leftarrow \tilde{d}_s'$ 
18: end loop

```

---

## 3. Analysis

Inserting the error parameters from both strategies into Eq. (3) yields the curves in Fig. 7.

*a. Feasibility range.* Strategy 2 requires all  $N_{\text{QEC}}$  pairs to survive in memory until surgery begins, so the no-expire condition demands

$$\eta_{\text{link}} \geq \eta_{\text{min}}^{\text{S2}} = \frac{N_{\text{QEC}}}{\ln(F_0/F_{\text{th}})}, \quad (\text{C5})$$

a bound  $d_s$  times tighter than Strategy 1's requirement  $\eta_{\text{min}}^{\text{S1}} = n^{\text{round}}/\ln(F_0/F_{\text{th}})$ . Strategy 1 therefore remains viable at link efficiencies a factor of  $d_s$  below what Strategy 2 requires.

*b. Strategy comparison.* The two strategies trade Bell-pair quality against idle noise. Strategy 2 eliminates the idle penalty ( $\tilde{p}_{\text{local}}^{\text{S2}} = p_{\text{phys}}$ ) but stores the earliest pair  $d_s$  times longer. From Eqs. (23) and (C4),

$$\frac{F_{\text{stored}}^{\text{S2}}}{F_{\text{stored}}^{\text{S1}}} = \exp\left(-\frac{(d_s - 1)n^{\text{round}}}{\eta_{\text{link}}}\right), \quad (\text{C6})$$

so Strategy 2's Bell-pair fidelity degrades exponentially with  $d_s$  relative to Strategy 1 at any fixed  $\eta_{\text{link}}$ . By contrast, Strategy 1's idle penalty  $p_{\text{idle}}$  (Eq. (C2)) depends on  $n^{\text{round}}/(\mu \eta_{\text{link}})$  and carries no analogous  $d_s$ -fold amplification.

Since both  $p_{\text{Bell}}$  and  $\tilde{p}_{\text{local}}$  enter the logical error rate (Eq. (3)) raised to an exponent that grows with  $d_s$ , the exponential fidelity gap between strategies is further amplified at larger code distance, whereas the moderate increase in  $\tilde{p}_{\text{local}}$  from idle noise has a comparatively weak effect. Full numerical evaluation of Eq. (3) confirms that Strategy 1 dominates across nearly the entire feasible parameter space (Fig. 7); at sufficiently large  $\eta_{\text{link}}$  both error contributions vanish and the two strategies converge.

We therefore adopt Strategy 1 as the default scheduling protocol throughout this work.

## 4. Numerical Simulation

We simulate a lattice-surgery merge-and-split cycle between two distance- $d_s$  rotated surface-code patches for  $d_s \in \{3, 5, 7\}$ . The circuit comprises one initialization round,  $d_s$  syndrome-extraction rounds with the seam active (the last of which is the split round), one post-split round, and final data-qubit readout. All local gate, measurement, and reset noise follows Table II with  $p_{\text{phys}} = 10^{-3}$ .

Each seam CX gate is realized by teleporting the gate through a shared Bell pair, consumed in the zigzag order shown in Fig. 1(c). The resulting effective noise channel on (ctrl, target) combines Bell-pair depolarization at rate  $p_{\text{Bell}}$  with five local operations each at rate  $p_{\text{phys}}$ , and is dominated by the Pauli terms  $I \otimes X$ ,  $Z \otimes I$ , and  $Z \otimes X$ . Non-seam CX gates carry only standard depolarizing noise (Table II).

For Strategy 1 the idle wait between syndrome rounds adds single-qubit depolarizing noise at rate  $p_{\text{idle}}$  (Eq. (C2)) on every data qubit before each of the  $d_s - 1$

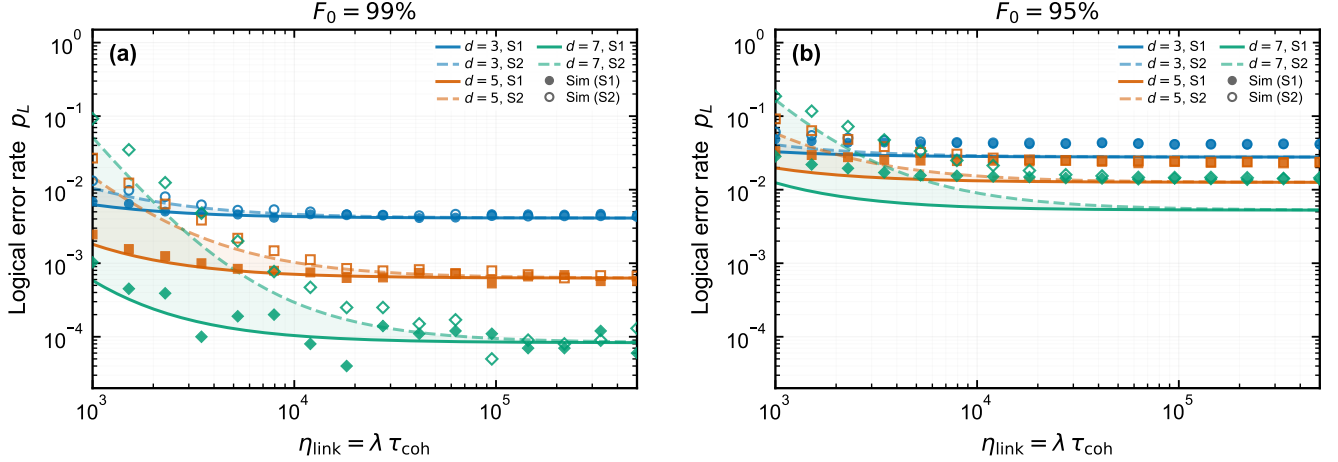


FIG. 7. **Logical error rate versus link efficiency  $\eta_{\text{link}}$  for Strategies 1 and 2 at  $d_s \in \{3, 5, 7\}$ .** Solid curves and filled markers: Strategy 1 (round-by-round); dashed curves and open markers: Strategy 2 (pre-buffered). Curves show an analytical model adapted from the fitted formula of Ref. [10], with the seam noise replaced by the effective teleported-CNOT Pauli channel; markers show Stim circuit-level simulation decoded with MWPM. Each simulation point is the basis-averaged logical error rate  $p_L = \frac{1}{2}(p_{L,ZZ} + p_{L,XX})$ , combining  $Z_L \otimes Z_L$  and  $X_L \otimes X_L$  merge circuits ( $5 \times 10^4$  shots per basis). Shaded regions highlight the S1-S2 performance gap; vertical dotted lines mark the crossover  $\eta^*$ . (a)  $F_0 = 0.99$ . (b)  $F_0 = 0.95$ . The simulation markers constitute the primary quantitative results; the analytical curves provide a qualitative guide whose accuracy degrades at larger  $d_s$  because the fitted formula was calibrated on a simpler noise model.

post-merge rounds. Results for  $\mu = 10$  are presented in Fig. 7.

At fixed initial fidelity  $F_0$  and local error rate  $p_{\text{phys}}$ , the noise budget of each strategy is primarily controlled by the dimensionless parameter  $\eta_{\text{link}} \equiv \lambda \tau_{\text{coh}}$ , which counts how many Bell pairs the source can deliver within one memory coherence time. Physically, a batch of  $n^{\text{round}}$  pairs takes time  $n^{\text{round}}/\lambda$  to collect; dividing by  $\tau_{\text{coh}}$  gives the fractional coherence consumed per round,  $n^{\text{round}}/\eta_{\text{link}}$ , which enters the fidelity decay (Eq. (23)) and, for Strategy 1, the idle error (Eq. (C2)). A larger  $\eta_{\text{link}}$  therefore means a faster source relative to decoherence, yielding lower  $p_{\text{Bell}}$  for both strategies and lower  $p_{\text{idle}}$  for Strategy 1. In the figures,  $\eta_{\text{link}}$  serves as the horizontal axis; for each value,  $p_{\text{Bell}}$  and (where applicable)  $p_{\text{idle}}$  are computed from Eqs. (23)–(C2) with  $F_0 \in \{0.99, 0.95\}$  and  $n^{\text{round}} = 2d_s - 1$  (Eq. (1)), then injected into the circuit as described above.

Both  $Z_L \otimes Z_L$  and  $X_L \otimes X_L$  merge circuits are simulated.  $\eta_{\text{link}}$  is swept over 16 logarithmically spaced points in  $[10^3, 5 \times 10^5]$ . Circuits are built in Stim [49] and decoded with minimum-weight perfect matching (Py-Matching [51]) using  $10^5$  total shots per  $(d_s, F_0, \eta_{\text{link}})$  point, split equally between  $Z_L \otimes Z_L$  and  $X_L \otimes X_L$ . The basis-averaged logical error rate is  $\text{LER} = \frac{1}{2}(\text{LER}_{ZZ} + \text{LER}_{XX})$ , where each  $\text{LER}_{\mathcal{B}}$  is the fraction of shots with at least one logical flip among the three observables  $\{O_L^{\text{left}}, O_L^{\text{right}}, O_L \otimes O_L\}$  in basis  $\mathcal{B}$ .

Figure 7 shows that S1 outperforms S2 at low-to-moderate  $\eta_{\text{link}}$ , where the shorter per-round storage time keeps Bell-pair fidelity significantly higher, despite the

additional idle depolarization  $p_{\text{idle}}(\eta_{\text{link}})$  on data qubits between rounds; as  $\eta_{\text{link}} \rightarrow \infty$  both Bell-pair noise and idle noise vanish, so the two strategies converge.

#### Appendix D: Physical Qubit Budget

Every module in a distributed architecture pays a fixed overhead in physical qubits before any logical encoding begins. Communication qubits are needed to interface with photonic links. Memory qubits are needed to buffer Bell pairs during stochastic generation. Distillation reduces code distance at the cost of higher per-pair consumption. In contrast, direct consumption avoids that consumption overhead but requires a larger code distance to tolerate raw noise. Consequently, which strategy yields more logical qubits from the same  $N_{\text{phy}}$  depends on the operating point.

##### a. Communication and Memory Qubits

*Communication qubits.* Each of the  $I$  optical interfaces requires dedicated qubits to mediate photon emission and heralded entanglement. The minimum number of qubits used to generate entanglement is therefore  $N_{\text{comm}} = I$  [52, 53]. When the attempt rate exceeds the inverse reset time, time-division multiplexing is required to maintain throughput, giving

$$N_{\text{comm}} = I \cdot \max(1, \lceil \tau_{\text{reset}} \cdot r_{\text{attempt}} \rceil). \quad (\text{D1})$$

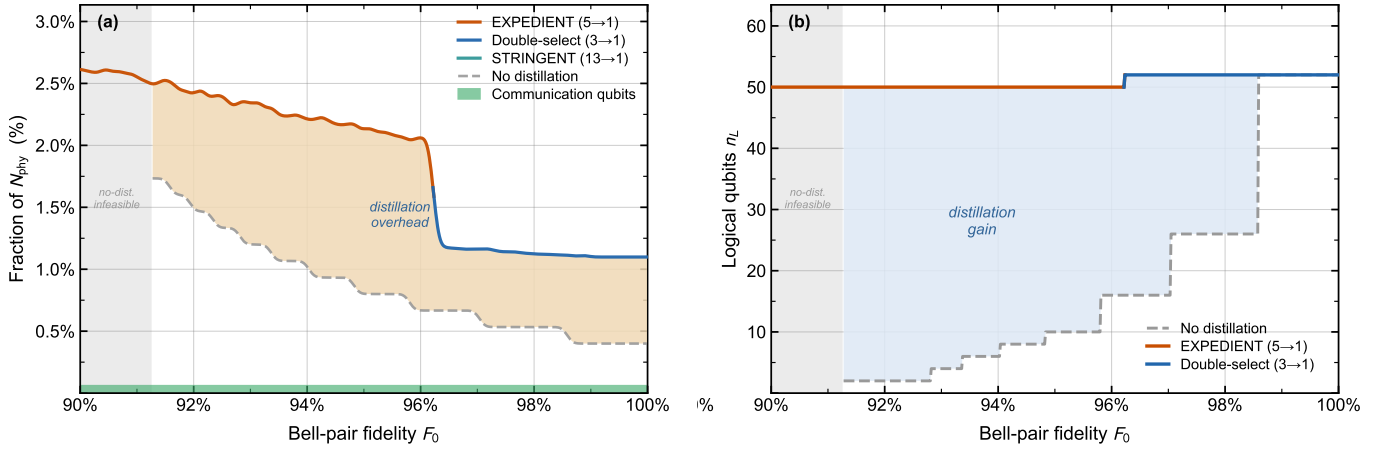


FIG. 8. **Physical qubit allocation per module vs. Bell-pair fidelity  $F_0$**  ( $N_{\text{phy}} = 3000$ ,  $p_L \leq 10^{-3}$ ). (a) Communication and memory physical qubit consumption per module. The green band shows the fixed communication overhead  $N_{\text{comm}}$  (Eq. (D1)), set to 2 optical interfaces; orange solid and yellow dashed lines show memory overhead  $N_{\text{mem}}$  under optimal distillation and no distillation, respectively (Eqs. (D3) and (D2)). The gray region marks the no-distillation infeasible zone ( $n_L < 2$ ). (b) Logical qubit capacity  $n_L$  (Eq. (D4)), computed on a two-column patch grid that accounts for inter-patch lattice-surgery overhead. Solid colored lines show the optimal distillation envelope (protocol with highest  $n_L$  at each  $F_0$ ); the blue band indicates distillation gain  $\Delta n_L > 0$ . Noise parameters are listed in Table II; surface-code distances  $d_s^*$  are computed following Sec. III A.

This count is set entirely by generation-layer hardware and is independent of code distance or distillation strategy.

*Memory qubits.* Each heralded pair occupies a memory qubit until it is consumed. We assume the conservative minimum occupancy, setting aside decay effects analyzed in Sec. IV.

Without distillation, the module stores one raw pair per seam qubit per syndrome round:

$$N_{\text{mem}}^{(\text{raw})} = n^{\text{round}}(p_{\text{raw}}) = a d_s^*(p_{\text{raw}}) - c. \quad (\text{D2})$$

with distillation, each of the  $n^{\text{round}}(p_{\text{eff}})$  purified pairs needed per round is produced by  $k$  parallel distillation circuits (Eq. (B2)), each holding  $n_{\text{pairs}}$  raw inputs simultaneously:

$$N_{\text{mem}}^{(\text{dist})} = n^{\text{round}}(p_{\text{eff}}) \times k \times n_{\text{pairs}}. \quad (\text{D3})$$

Whether  $N_{\text{mem}}^{(\text{dist})}$  exceeds  $N_{\text{mem}}^{(\text{raw})}$  depends on whether the distance reduction from distillation compensates for the  $k \times n_{\text{pairs}}$  multiplier.

### b. Logical Qubit Capacity

A distance- $d$  rotated surface code requires  $2d^2 - 1$  physical qubits per patch ( $d^2$  data,  $d^2 - 1$  ancilla); ancilla-reuse schemes [54] reduce this to  $\approx 1.5d^2$ , though we adopt the conservative count. Lattice surgery between adjacent patches requires  $d$  additional physical qubits along each shared boundary. For simplicity we consider a two-column patch grid, in which  $n_L/2$  rows share  $\frac{3}{2}n_L - 2$

internal boundaries. After subtracting overhead, a module hosts

$$n_L = 2 \left[ \frac{N_{\text{phy}} - N_{\text{comm}} - N_{\text{mem}} + 2d_s^*}{4(d_s^*)^2 + 3d_s^* - 2} \right] \quad (\text{D4})$$

logical qubits. The denominator grows as  $(d_s^*)^2$ , so lowering  $p_L^{\text{target}}$  quadratically compresses logical capacity even before overhead is accounted for.

Distillation reduces  $d_s^*$ ; to leading order the capacity gain is  $\Delta n_L \approx n_L^{\text{raw}}(\rho^{-2} - 1)$  where  $\rho = d_s^{\text{dist}}/d_s^{\text{raw}}$  (Eq. (9)), though the actual gain is moderated by the increased memory overhead  $N_{\text{mem}}$ .

### c. Budget Constraint

The total physical qubit count per module satisfies

$$N_{\text{phy}} = \underbrace{n_L(2(d_s^*)^2 - 1) + \left(\frac{3}{2}n_L - 2\right)d_s^*}_{\text{logical grid}} + N_{\text{comm}} + N_{\text{mem}}. \quad (\text{D5})$$

Distillation shrinks the grid term through a smaller  $d_s^*$  but inflates  $N_{\text{mem}}$  through the  $k \times n_{\text{pairs}}$  multiplier; the optimal strategy at each  $F_0$  is the one that maximises  $n_L$ . Figure 8 shows how the allocation shifts across operating regimes.

## Appendix E: Transversal Methods

An alternative approach for DQC involves distributed transversal operations, as detailed in [5]. A comprehensive comparison is outside the scope of this work and

is complicated by the differences in compilation methods between lattice surgery and transversal approaches. But, transversal methods generally require  $n$  Bell pairs to be available for simultaneous consumption for an  $[n, k, d]$  code [5]. This contrasts with the lattice surgery methods discussed in this paper, which typically require fewer

simultaneous pairs, although the cumulative Bell pair count across all rounds is likely higher. That being said, transversal operations on dense qLDPC codes enable parallel non-local CNOTs between or teleportation of multiple logical qubits, significantly lowering the number of Bell pairs used per logical operation [5].

- 
- [1] H. Jacinto, Élie Gouzien, and N. Sangouard, Network requirements for distributed quantum computation (2025), arXiv:2504.08891 [quant-ph].
- [2] J. Ramette, J. Sinclair, N. P. Breuckmann, and V. Vuletić, Fault-tolerant connection of error-corrected qubits with noisy links, *npj Quantum Information* **10**, 58 (2024), arXiv:2302.01296 [quant-ph].
- [3] M. A. Shalby, R. Wang, D. Sedov, and L. P. Pryadko, Optimized noise-resilient surface code teleportation interfaces (2025), arXiv:2503.04968 [quant-ph].
- [4] T. H. Haug, T. Hillmann, A. F. Kockum, and R. V. Laer, Lattice surgery with bell measurements: Modular fault-tolerant quantum computation at low entanglement cost (2025), arXiv:2510.13541 [quant-ph].
- [5] J. Stack, M. Wang, and F. Mueller, Assessing teleportation of logical qubits in a distributed quantum architecture under error correction (2025), arXiv:2504.05611 [quant-ph].
- [6] W. Dür and H. J. Briegel, Entanglement purification for quantum computation., *Physical review letters* **90**, 067901 (2002).
- [7] P. Pathumsoot, T. Tansuwannont, N. Benchasattabuse, R. Satoh, M. Hajdušek, P. Chaiwongkhot, S. Suwanna, and R. Van Meter, Boosting End-to-End Entanglement Fidelity in Quantum Repeater Networks via Hybridized Strategies (2024) arXiv:2406.06545 [quant-ph].
- [8] H. Leone, T. Le, S. Srikara, and S. Devitt, Resource overheads and attainable rates for trapped-ion lattice surgery (2024), arXiv:2406.18764 [quant-ph].
- [9] S. de Bone, P. Möller, C. E. Bradley, T. H. Taminiau, and D. Elkouss, Thresholds for the distributed surface code in the presence of memory decoherence, *AVS Quantum Science* **6**, 10.1116/5.0200190 (2024).
- [10] S. Sunami, Y. Hirano, T. Hinokuma, and H. Yamasaki, Entanglement boosting: Low-volume logical bell pair preparation for distributed fault-tolerant quantum computation (2025), arXiv:2511.10729 [quant-ph].
- [11] D. Litinski, A Game of Surface Codes: Large-Scale Quantum Computing with Lattice Surgery, *Quantum* **3**, 128 (2019).
- [12] D. Horsman, A. G. Fowler, S. Devitt, and R. Van Meter, Surface code quantum computing by lattice surgery, *New Journal of Physics* **14**, 123011 (2012).
- [13] D. Litinski and F. v. Oppen, Lattice Surgery with a Twist: Simplifying Clifford Gates of Surface Codes, *Quantum* **2**, 62 (2018).
- [14] S. Liu, N. Benchasattabuse, D. Q. Morgan, M. Hajdušek, S. J. Devitt, and R. Van Meter, A substrate scheduler for compiling arbitrary fault-tolerant graph states, in *2023 IEEE International Conference on Quantum Computing and Engineering (QCE)*, Vol. 01 (2023) pp. 870–880.
- [15] D. L. Moehring, P. Maunz, S. Olmschenk, K. C. Younge, D. N. Matsukevich, L. M. Duan, and C. Monroe, Entanglement of single-atom quantum bits at a distance, *Nature* **449**, 68 (2007).
- [16] C. Monroe, R. Raussendorf, A. Ruthven, K. R. Brown, P. Maunz, L.-M. Duan, and J. Kim, Large-scale modular quantum-computer architecture with atomic memory and photonic interconnects, *Physical Review A* **89**, 10.1103/physreva.89.022317 (2014).
- [17] L. J. Stephenson, D. P. Nadlinger, B. C. Nichol, S. An, P. Drmota, T. G. Ballance, K. Thirumalai, J. F. Goodwin, D. M. Lucas, and C. J. Ballance, High-rate, high-fidelity entanglement of qubits across an elementary quantum network, *Phys. Rev. Lett.* **124**, 110501 (2020).
- [18] D. Awschalom, K. K. Berggren, H. Bernien, S. Bhave, L. D. Carr, P. Davids, S. E. Economou, D. Englund, A. Faraon, M. Fejer, S. Guha, M. V. Gustafsson, E. Hu, L. Jiang, J. Kim, B. Korzh, P. Kumar, P. G. Kwiat, M. Lončar, M. D. Lukin, D. A. Miller, C. Monroe, S. W. Nam, P. Narang, J. S. Orcutt, M. G. Raymer, A. H. Safavi-Naeini, M. Spiropulu, K. Srinivasan, S. Sun, J. Vučković, E. Waks, R. Walsworth, A. M. Weiner, and Z. Zhang, Development of quantum interconnects (quics) for next-generation information technologies, *PRX Quantum* **2**, 017002 (2021).
- [19] P. C. Humphreys, N. Kalb, J. P. J. Morits, R. N. Schouten, R. F. L. Vermeulen, D. J. Twitchen, M. Markham, and R. Hanson, Deterministic delivery of remote entanglement on a quantum network, *Nature* **558**, 268 (2018), arXiv:1712.07567 [quant-ph].
- [20] P. Dhara, D. Englund, and S. Guha, Entangling quantum memories via heralded photonic bell measurement, *Phys. Rev. Res.* **5**, 033149 (2023).
- [21] S. Saha, M. Shalaev, J. O'Reilly, I. Goetting, G. Toh, A. Kalakuntla, Y. Yu, and C. Monroe, High-fidelity remote entanglement of trapped atoms mediated by time-bin photons, *Nature Communications* **16**, 10.1038/s41467-025-57557-4 (2025).
- [22] M. DeCross, R. Haghshenas, M. Liu, E. Rinaldi, J. Gray, Y. Alexeev, C. Baldwin, J. Bartolotta, M. Bohn, E. Chertkov, J. Cline, J. Colina, D. DelVento, J. Dreiling, C. Foltz, J. Gaebler, T. Gatterman, C. Gilbreth, J. Giles, D. Gresh, A. Hall, A. Hankin, A. Hansen, N. Hewitt, I. Hoffman, C. Holliman, R. Hutson, T. Jacobs, J. Johansen, P. Lee, E. Lehman, D. Lucchetti, D. Lykov, I. Madjarov, B. Mathewson, K. Mayer, M. Mills, P. Niroula, J. Pino, C. Roman, M. Schecter, P. Siegfried, B. Tiemann, C. Volin, J. Walker, R. Shaydulin, M. Pistoia, S. Moses, D. Hayes, B. Neyenhuis, R. Stutz, and M. Foss-Feig, Computational power of random quantum circuits in arbitrary geometries, *Physical Review X* **15**, 10.1103/physrevx.15.021052 (2025).
- [23] C. J. Ballance, T. P. Harty, N. M. Linke, M. A. Sepiol, and D. M. Lucas, High-fidelity quantum logic gates using trapped-ion hyperfine qubits, *Phys. Rev. Lett.* **117**,

- 060504 (2016).
- [24] J. Schupp, V. Krcmarsky, V. Krutyanskiy, M. Meraner, T. Northup, and B. Lanyon, Interface between trapped-ion qubits and traveling photons with close-to-optimal efficiency, *PRX Quantum* **2**, 020331 (2021).
- [25] H. Takahashi, E. Kassa, C. Christoforou, and M. Keller, Strong coupling of a single ion to an optical cavity, *Physical Review Letters* **124**, 10.1103/physrevlett.124.013602 (2020).
- [26] A. G. Fowler, M. Mariantoni, J. M. Martinis, and A. N. Cleland, Surface codes: Towards practical large-scale quantum computation, *Physical Review A* **86**, 10.1103/physreva.86.032324 (2012).
- [27] S. Krastanov, V. V. Albert, and L. Jiang, Optimized Entanglement Purification, *Quantum* **3**, 123 (2019).
- [28] K. Fujii and K. Yamamoto, Entanglement purification with double selection, *Phys. Rev. A* **80**, 042308 (2009).
- [29] N. H. Nickerson, Y. Li, and S. C. Benjamin, Topological quantum computing with a very noisy network and local error rates approaching one percent, *Nature Commun.* **4**, 1756 (2013), arXiv:1211.2217 [quant-ph].
- [30] C. H. Bennett, G. Brassard, S. Popescu, B. Schumacher, J. A. Smolin, and W. K. Wootters, Purification of noisy entanglement and faithful teleportation via noisy channels, *Phys. Rev. Lett.* **76**, 722 (1996).
- [31] D. Deutsch, A. Ekert, R. Jozsa, C. Macchiavello, S. Popescu, and A. Sanpera, Quantum privacy amplification and the security of quantum cryptography over noisy channels, *Phys. Rev. Lett.* **77**, 2818 (1996).
- [32] J. O'Reilly, G. Toh, I. Goetting, S. Saha, M. Shalaev, A. L. Carter, A. Risinger, A. Kalakuntla, T. Li, A. Verma, and C. Monroe, Fast photon-mediated entanglement of continuously cooled trapped ions for quantum networking, *Phys. Rev. Lett.* **133**, 090802 (2024).
- [33] D. Hucul, I. V. Inlek, G. Vittorini, C. Crocker, S. Deb Nath, S. M. Clark, and C. Monroe, Modular entanglement of atomic qubits using photons and phonons, *Nature Physics* **11**, 37 (2015), arXiv:1403.3696 [quant-ph].
- [34] L. Bacciottini, M. G. D. Andrade, S. Pouryoucef, E. A. V. Milligen, A. Chandra, N. K. Panigrahy, N. S. V. Rao, G. Vardoyan, and D. Towsley, Leveraging internet principles to build a quantum network, *IEEE Network*, 1–1 (2025).
- [35] J. Halder, E. Matus, and G. Fettweis, On the concurrent multipath entanglement distribution in quantum networks, in *GLOBECOM 2024 - 2024 IEEE Global Communications Conference* (2024) pp. 2791–2796.
- [36] J. Grimbergen, S. Haldar, A. G. Inesta, and S. Wehner, Probabilistic cutoffs in homogeneous quantum repeater chains (2026), arXiv:2602.14738 [quant-ph].
- [37] I. Yakar and M. Ben-Or, Advantages of global entanglement-distillation policies in quantum repeater chains (2025), arXiv:2510.06737 [quant-ph].
- [38] P. Drmota, D. Main, D. P. Nadlinger, B. C. Nichol, M. A. Weber, E. M. Ainley, A. Agrawal, R. Srinivas, G. Araneda, C. J. Ballance, and D. M. Lucas, Robust quantum memory in a trapped-ion quantum network node, *Phys. Rev. Lett.* **130**, 090803 (2023).
- [39] P. Wang, C.-Y. Luan, M. Qiao, M. Um, J. Zhang, Y. Wang, X. Yuan, M. Gu, J. Zhang, and K. Kim, Single ion qubit with estimated coherence time exceeding one hour, *Nature Communications* **12**, 10.1038/s41467-020-20330-w (2021).
- [40] J. M. Pino, J. M. Dreiling, C. Figgatt, J. P. Gaebler, S. A. Moses, M. S. Allman, C. H. Baldwin, M. Foss-Feig, D. Hayes, K. Mayer, C. Ryan-Anderson, and B. Neyenhuis, Demonstration of the trapped-ion quantum ccd computer architecture, *Nature* **592**, 209–213 (2021).
- [41] S. Dasu, M. DeCross, A. Y. Guo, A. Lavasani, J. Behrends, A. Benhemou, Y.-H. Chen, K. Mayer, C. N. Self, S. Simsek, B. Srivastava, M. S. Allman, J. Arkininstall, J. G. Bohnet, N. Q. Burdick, J. P. C. III, A. Chernoguzov, S. F. Cooper, R. D. Delaney, J. M. Dreiling, B. Estey, C. Figgatt, C. Foltz, J. P. Gaebler, A. Hall, C. A. Holliman, A. A. Husain, A. Isanaka, C. J. Kennedy, Y. Kodama, N. Kotibhaskar, N. K. Lysne, I. S. Madjarov, M. Mills, A. R. Milne, B. Neyenhuis, A. J. Park, A. Ransford, A. P. Reed, S. J. Sanders, C. H. Baldwin, D. Hayes, B. Criger, A. C. Potter, and D. Amaro, Computing with many encoded logical qubits beyond break-even (2026), arXiv:2602.22211 [quant-ph].
- [42] W. Zhang, T. van Leent, K. Redeker, R. Garthoff, R. Schwonnek, F. Fertig, S. Eppelt, W. Rosenfeld, V. Scarani, C. C.-W. Lim, and H. Weinfurter, A device-independent quantum key distribution system for distant users, *Nature* **607**, 687–691 (2022).
- [43] L. Hartung, M. Seubert, S. Welte, E. Distanto, and G. Rempe, A quantum-network register assembled with optical tweezers in an optical cavity, *Science* **385**, 179–183 (2024).
- [44] A. Safari, E. Oh, P. Huft, G. Chase, J. Zhang, and M. Saffman, Efficient and compact quantum network node based on a parabolic mirror on an optical chip (2026), arXiv:2601.13420 [quant-ph].
- [45] L. Li, X. Hu, Z. Jia, W. Huie, W. K. C. Sun, Aakash, Y. Dong, N. Hiri-O-Tuppa, and J. P. Covey, Parallelized telecom quantum networking with an ytterbium-171 atom array, *Nature Physics* **21**, 1826–1833 (2025).
- [46] Y. Li and J. D. Thompson, High-rate and high-fidelity modular interconnects between neutral atom quantum processors, *PRX Quantum* **5**, 020363 (2024).
- [47] H. J. Manetsch, G. Nomura, E. Bataille, X. Lv, K. H. Leung, and M. Endres, A tweezer array with 6,100 highly coherent atomic qubits, *Nature* **647**, 60 (2025), arXiv:2403.12021 [quant-ph].
- [48] D. Bluvstein, S. J. Evered, A. A. Geim, S. H. Li, H. Zhou, T. Manovitz, S. Ebadi, M. Cain, M. Kalinowski, D. Hangleiter, J. P. Bonilla Ataides, N. Maskara, I. Cong, X. Gao, P. Sales Rodriguez, T. Karolyshyn, G. Semeghini, M. J. Gullans, M. Greiner, V. Vuletić, and M. D. Lukin, Logical quantum processor based on reconfigurable atom arrays, *Nature* **626**, 58–65 (2023).
- [49] C. Gidney, Stim: a fast stabilizer circuit simulator, *Quantum* **5**, 497 (2021).
- [50] J. P. Bonilla Ataides, H. Zhou, Q. Xu, G. Baranes, B. Li, M. D. Lukin, and L. Jiang, Constant-overhead fault-tolerant bell-pair distillation using high-rate codes, *Physical Review Letters* **135**, 10.1103/s39k-r2kq (2025).
- [51] O. Higgott, Pymatching: A python package for decoding quantum codes with minimum-weight perfect matching, *ACM Transactions on Quantum Computing* **3**, 1 (2022).
- [52] S. Singh, F. Gu, S. de Bone, E. Villaseñor, D. Elkouss, and J. Borregaard, Modular architectures and entanglement schemes for error-corrected distributed quantum computation, *npj Quantum Information* **12**, 10.1038/s41534-025-01146-2 (2025).

- [53] D. Main, P. Drmota, D. P. Nadlinger, E. M. Ainley, A. Agrawal, B. C. Nichol, R. Srinivas, G. Araneda, and D. M. Lucas, Distributed quantum computing across an optical network link, *Nature* **638**, 383–388 (2025).
- [54] A. Chatterjee, A. Ghosh, and S. Ghosh, Quantum prometheus: Defying overhead with recycled ancillas in quantum error correction, in *2025 26th International Symposium on Quality Electronic Design (ISQED)* (2025) pp. 1–7.